My Present Research Interests

1. Corrosion Cracking in Concrete

Corrosion is a subsidiary problem of reinforced concrete (RC) structures, which are subjected to salt attack. It is known as one of the major deterioration mechanisms in RC structures (Ohtsu et al., 1997). Because concrete is a porous material, carbon dioxide and chloride can easily penetrate into it. As a result, the passivity of the steel is destroyed, and then the reinforcement in concrete is corroded. As shown in Figure 1, expansion of corrosion products generates cracks which result in serious defects in RC structures. There are two kinds of rebar corrosions, chloride-induced corrosion and carbonation-induced corrosion (Hansson, 1995). Generally speaking, chloride-induced corrosion is more serious than carbonation-induced corrosion. Chloride can get into the concrete at the time of concrete mixing or can penetrate into the hardened concrete later on. For the case of chloride in the surrounding environmental penetrating into the concrete, a sufficient quantity of chloride ions must first be accumulated. Next, a localized breakdown of the passive film on the rebar is formed by the action of these accumulated chloride ions and thus a galvanic cell is created. The local active areas behave as anodes, while the remaining passive areas become cathodes where reduction of dissolved oxygen takes place. As the rebar increases its state of oxidation, the volume of the corrosion products expands. The unit volume of iron (Latin word –ferrum (Fe)) can be doubled if ferrous oxide (FeO) formed. The unit volume of the final corrosion product, $Fe(OH)_3.3H_2O$, is as large as six and a half times of the original Fe volume (Li et al., 1998). This expansion creates cracking and spalling inside concrete, finally destroy the integrity of the structural concrete and cause a failure of building and infrastructures.

As a result of the hydration reactions of cement, the pore solution of concrete tends to be alkaline, with pH values typically in the range 12.5-13.6. Under such alkaline conditions, reinforcing steel tends to be passive and denotes negligible corrosion rates. However, due to the porous nature of concrete, corrosive and chemical species responsible for corrosion can enter the concrete and lead to corrosion problems. Furthermore, corrosive species could enter the mix if "contaminated" ingredients are mixed in water, aggregates, and additives.

Figure 1 Corrosion damage in an elevated highway structure.

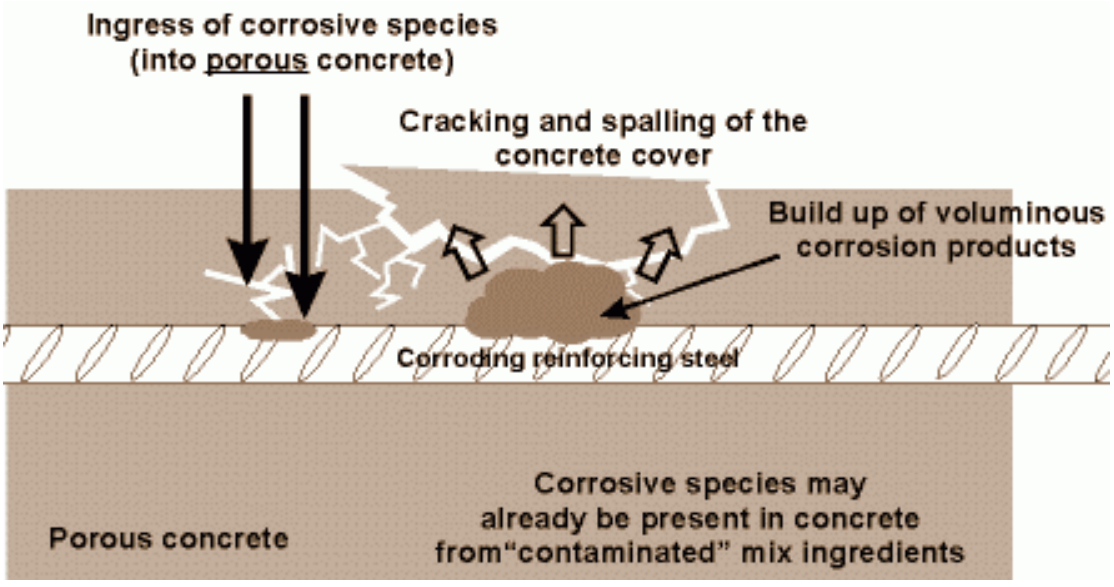

Figure 2 Schematic diagram of cracking and spalling in concrete.

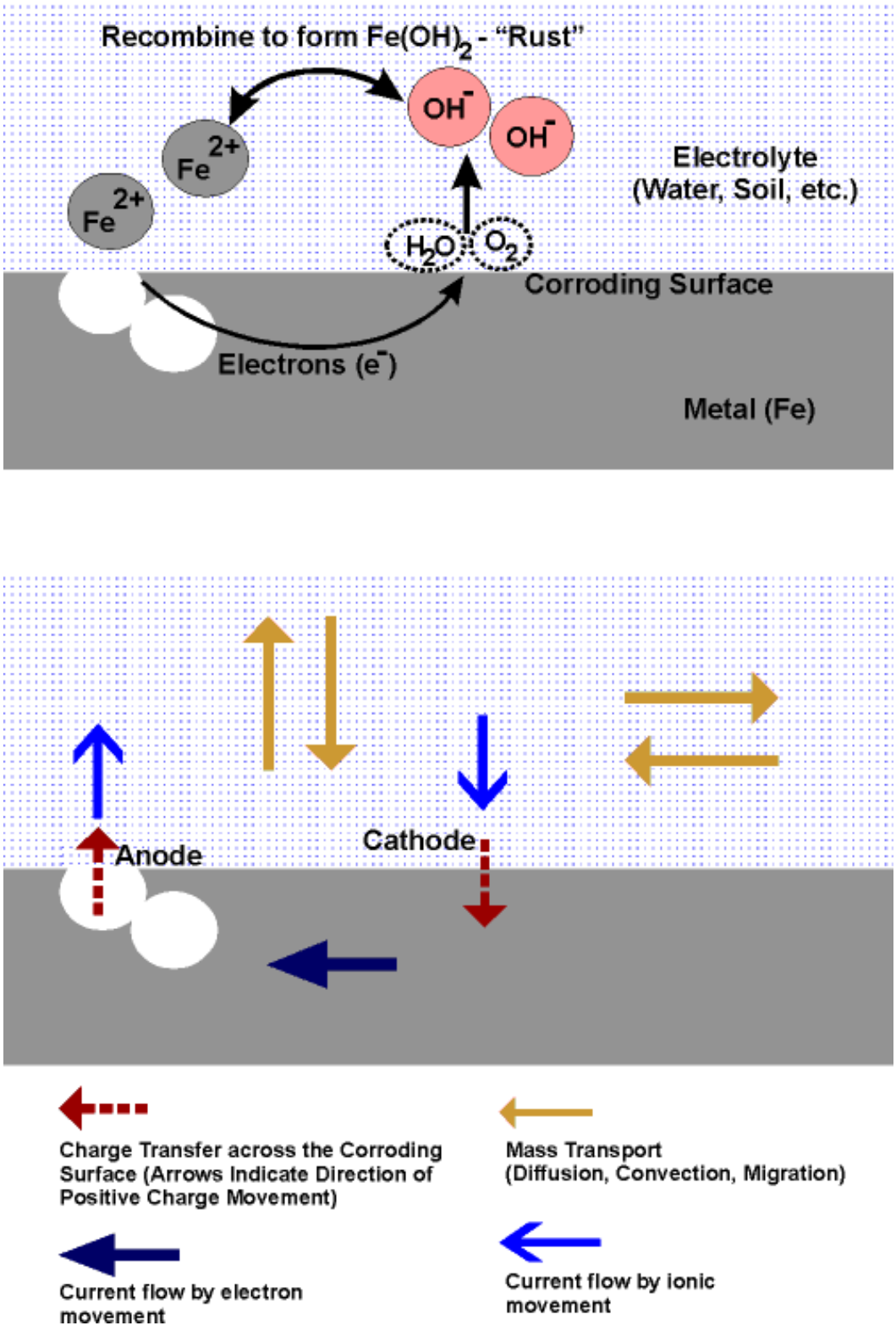

Figure 3 Schematic representation of electrochemical corrosion process (aqueous corrosion of iron under near neutral pH conditions).

Corrosion of the reinforcing steel results in the build-up of voluminous corrosion products, generating internal stresses and subsequent cracking and spalling of the concrete as shown schematically in Figure 2 (Tullmin, 2003). Clearly the reinforcing steel is more vulnerable to further corrosion damage after the protective concrete cover is compromised in this manner.

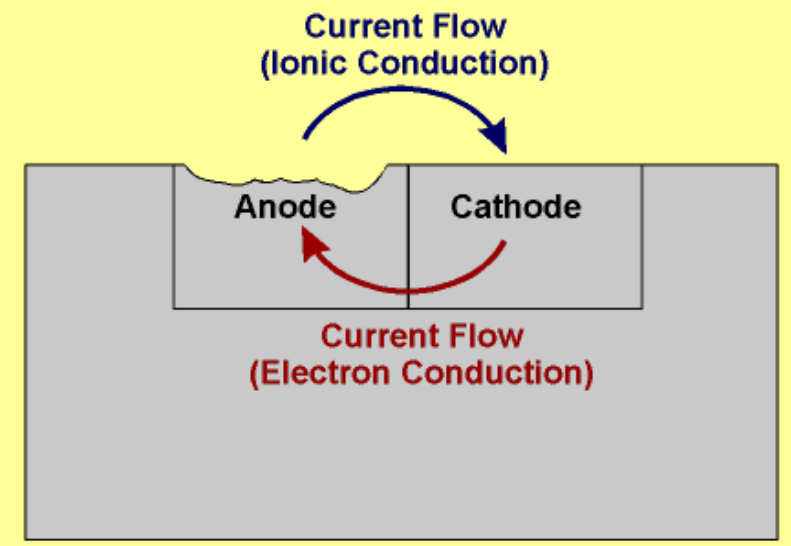

Figure 4 Schematic representation of current flow (conventional current direction) in a simple corrosion cell.

According to the electrochemical corrosion theory in Figure 3 (Tullmin, 2003), the corrosion involves two half-cell reactions of an oxidation reaction at the anode and a reduction reaction at the cathode. For iron corroding in water with a near neutral pH, these half-cell reactions can be represented as,

Anode reaction: $2Fe \Rightarrow 2Fe^{2+} + 4e^{-}$

Cathode reaction: $O_2 + 2H_2O + 4e^{-} \Rightarrow 4OH^{-}$

There are obviously different anodic and cathodic reactions for different alloys exposed to various environments. These half-cell reactions are thought to occur (at least initially) at microscopic anodes and cathodes on a corroding surface. Macroscopic anodes and cathodes can

develop as corrosion damage progresses with time. From the theory there are four fundamental components in an electrochemical corrosion cell,

1. An anode.
2. A cathode.
3. A conducting environment for ionic movement (electrolyte).
4. An electrical connection between the anode and cathode for the flow of electron current.

If any of the above components is missing or disabled, the electrochemical corrosion process may be stopped.

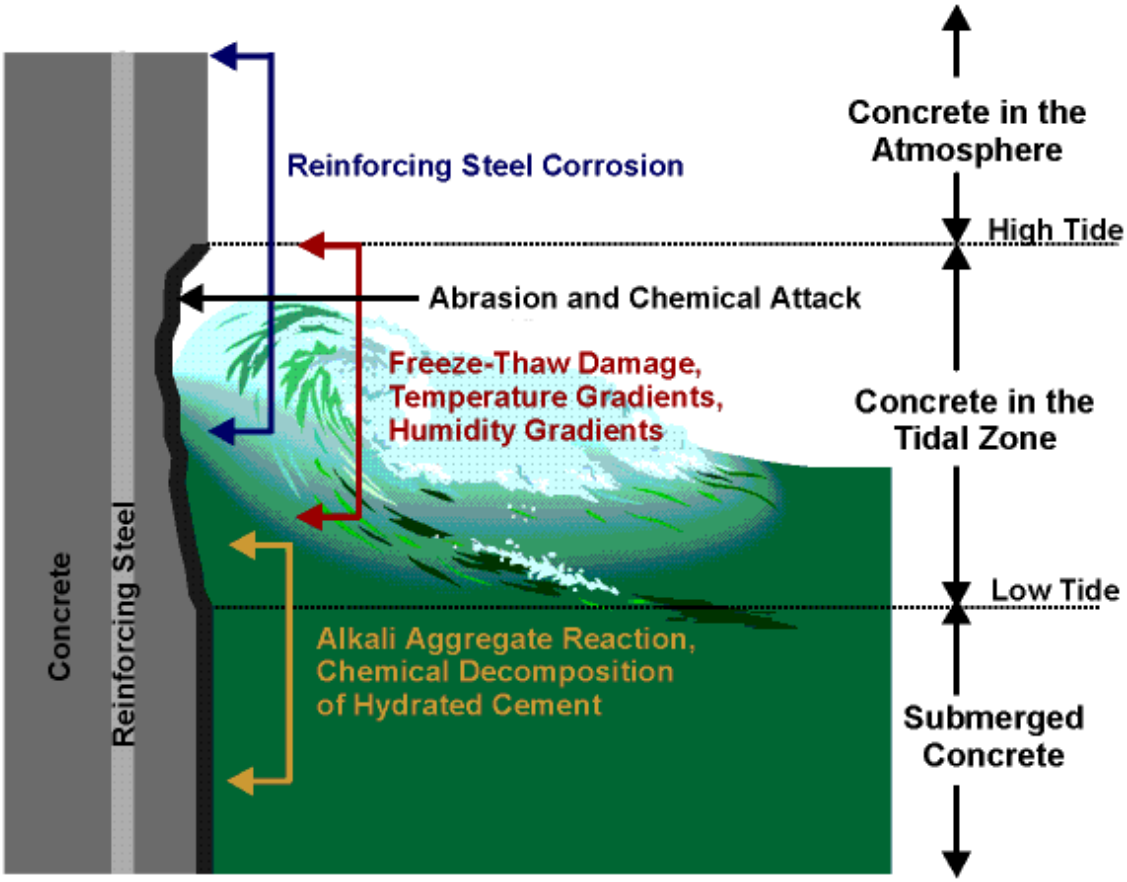

Figure 5 Schematic representations of the degradation mechanisms on concrete exposed to seawater.

Concrete durability has been defined by the American Concrete Institute (Tullmin, 2003) as its resistance to weathering action, chemical attack, abrasion and other degradation processes. In Figure 4 (Tullmin, 2003), a schematic representation of current flow (conventional current direction) in a simple corrosion cell is shown, which is comparable to Figure 1.3.

In practice, several degradation mechanisms can act simultaneously with possible synergistic effects. The schematic diagram in Figure 5 (Tullmin, 2003) illustrates how different degradation mechanisms can act on concrete exposed to seawater.

The following images are taken at reinforced concrete wall of a bridge illustrate visual stages of the corrosion damage (Tullmin, 2003). The structure was built in 1979 and has been repeatedly subject to deicing salts in winter.

Stage 1: After construction, the concrete appears to be sound with relatively little macroscopic cracking and no reddish discoloration due to corrosion product.

Stage 2: Macroscopic cracks have appeared and the concrete surface is stained by reddish corrosion products.

Stage 3: Spalling of the concrete cover is found, due to the formation of voluminous corrosion products.

Scope of My Current Research

During more than two decades numerous researchers have studied the phenomenon of crack due to corrosion of reinforcement in concrete intensively (Ohtsu et al., 1997; Li et al., 1998).

Stage 4: Severe spalling of the concrete cover is evident, leaving the reinforcing steel bars directly exposed to the atmosphere.

Stage 5: Overall view of the concrete degradation in the wall. Spalling of the concrete and uncovered reinforcing steel is observed.

Various types of experiments were conducted, and the results were used to verify models that mostly deal with the crack kinematics based on fracture mechanics. The principle of energy equilibrium of the crack propagation in brittle material (Griffith, 1920) and the idea on the crack-extension force (Irwin, 1957) established the basic of fracture mechanics. The theory of cohesive cracks is introduced by considering attractive atomic forces in small region near the crack tip (Barenblatt, 1959). The first applications on fracture characteristic of concrete began by introducing of linear elastic fracture mechanics (LEFM) concepts to concrete (Neville, 1959; Kaplan, 1961). Dugdale (1960) proposed a mathematically similar but conceptually different model with a finite crack tip stress. An interpretation of these concepts proposed for the path independent

J-integral theory (Rice, 1968). Mindess (1983a,b) introduced a historical review and an annotated bibliography of the application of fracture mechanics to concrete.

For a better understanding to study the behaviour of a composite material like concrete, a so-called three level approach which defines three structural levels of observation and modeling of concrete can be followed (Wittmann, 1983). Inherent to this approach is the definition of three levels of observation: the micro-, meso- and macro-level. With the help of the processes which take place at a certain level, observations can be explained which are made one level higher. To set the scene, the micro-level takes into account the physical and chemical processes at the molecular level in the hardened cement paste, which is itself highly heterogeneous, incorporating the incorporates size up to approximately 10^{-4} meter. This level is not suited for fracture mechanics application in concrete. The meso-level considers the composite nature of concrete, which reaches sizes of 10^{-1} meter and distinguishes between hardened cement paste, inclusions, and the bond layer between them. Fracture mechanics may be applied at this level, but it does not reach the level of practical application. Even larger sizes belong to the macro-level.

It is realized that the fracture process zone is created ahead of the crack in concrete as shown in Figure 6. As a result, the non-linear fracture mechanics (NLFM) was introduced instead of LEFM (Hillerborg et al., 1976). Although most efforts have been lately devoted to characterize the fracture process zone (FPZ) physically and mechanically, LEFM seems to be still useful for studying the failure of concrete. In NLFM, the damaged zone material is assumed to exist ahead of the crack tip/front, in which the stored energy is gradually dissipated. In contrast, the maximum circumferencial stress criterion (Erdogan and SiH, 1963) based on LEFM was successfully applied to trace the crack extension of mixed-mode cracking (Ohtsu, 1988; Chahrour et al., 1992, 1993, 1994). By employing the two-domain BEM (boundary element method), crack orientations were evaluated from the stress intensity factors of mode I and mode II. The shift of dominant failure mode from mode I to mode II was observed, although crack extension was in principle governed by mode I cracking.

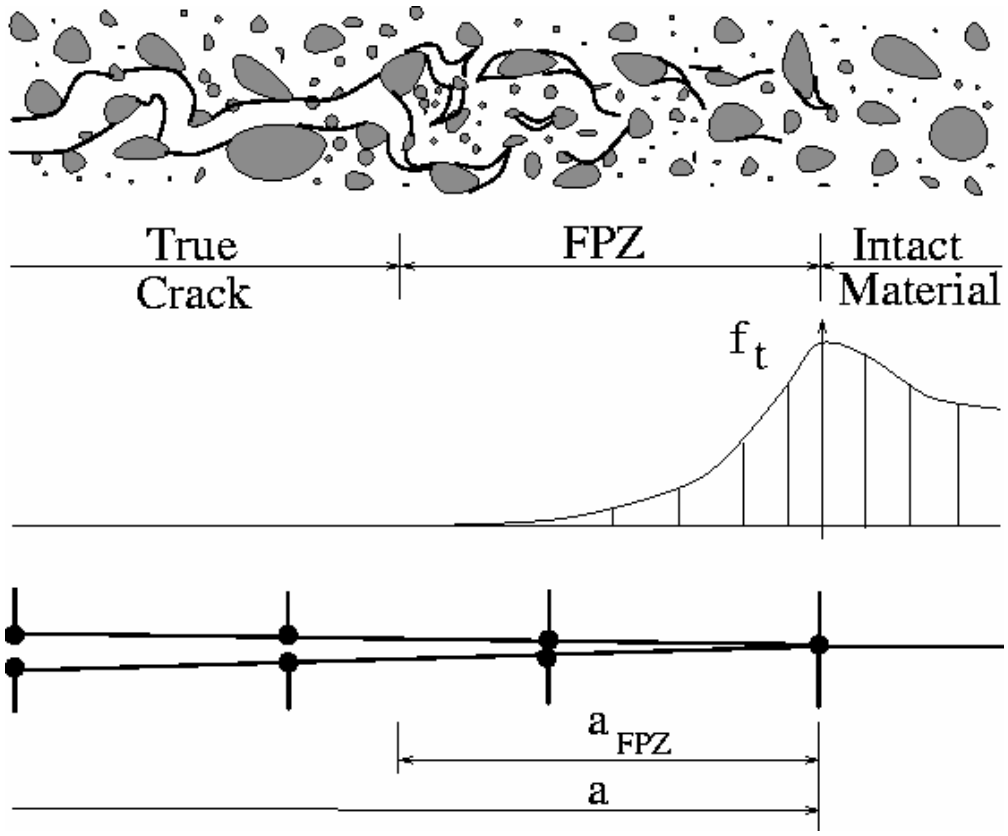

Figure 6 Fracture Process Zone in concrete.

The prime objective of the present study is to get more insight into the mechanisms underlying crack propagation due to corrosion of reinforcement in concrete. For making decision on maintenance and repair in reinforcement concrete, identification of cracking mechanisms due to corrosion is significantly important. Expansion caused by corrosion product generates cracking, of which mechanisms can be clarified analytically by BEM based on fracture mechanics.

In regard to the analysis, BEM deals with discretization of only the boundary and holds a privileged applicability to the discrete crack models. In this respect, the two-domain BEM is employed to simulate mode I and mixed mode fractures in plain concrete structures.

The effect of cracks on structural integrity is closely dependent on the location and the orientation of cracks. For example, initiation of tensile cracks perpendicular to the reinforcement is not as critical as diagonal shear cracks. The classification of crack types and the determination of crack orientations can be practically conducted by acoustic emission (AE) technique in addition to the locations.

2. Fracture Mechanics in Concrete and Application of Acoustic Emission Technique

Fracture mechanics in concrete

Fracture mechanics has been in use since neolithic times when man invented and designed simple and later more sophisticated stone tools. It is doubtful that these early ancestors of modern man did understand the mechanism of fracturing. In any case, they developed very skillful techniques how to shape and form blades, adzes and other stone tools which served their needs (Cotterell and Kaminga, 1990).

Several fracture related incidences which occurred in 12^{th} and 13^{th} century Europe are documented in the literature. Early quality control and testing of cannon bronze were accomplished by charging an up-side-down placed cannon and letting the gun barrel be thrown into the air. If, upon fall of the tube there was no crack or complete fracture the material was considered tough enough and the cannon could safely be put to service. Otherwise, this dynamic fracture test resulted in a broken cannon tube and the military device was in need of a re-cast.

In the first historically recorded study of fracture strength pertains to the measurement of the strength of iron wire by Leonardo da Vinci (1452-1519). A notebook of da Vinci shows a sketch of the loading system employed by Leonardo. The apparatus was redesigned and employed a basket that received a flow of fine sand from a hopper through an orifice. The flow of sand into the basket stopped abruptly when the wire broke as a spring was actuated to close the orifice. Da Vinci's comments supplied adjacent to the sketch have the appearance of instructions for testing. Apparently, da Vinci was attempting more than a simple proof test. The words 'more weight' correspond to the fact that the shortened length of 'this' wire must be stronger than the region previously separated. The repeated association of the fracture load with 'place in which it breaks' suggests an attempt to estimate the reduction of fracture strength from the appearance of the local region at the failure site. Iron wires available in the 15^{th} century were not of very high quality if one considers the way wires were drawn. A contemporary engraving shows a technician sitting on a water-power driven swing equipped with a pair of pliers for pulling the wire through an orifice with

each pull back of the swing. This technique results in thermally influenced inhomogeneities in the quality of the wire depending on the excursion of the swing. Plausible appearance features would include clamping indentations as well as local reduction in the diameter of the wire. Clearly, da Vinci's experiments illustrated the effect of flaws on strength. However, by using the pre-tested specimen fractions the quality of the wire at large could not be tested and Leonardo's particular way of shortening and reusing the already tested specimen fractions did not allow him to detect any true size effect.

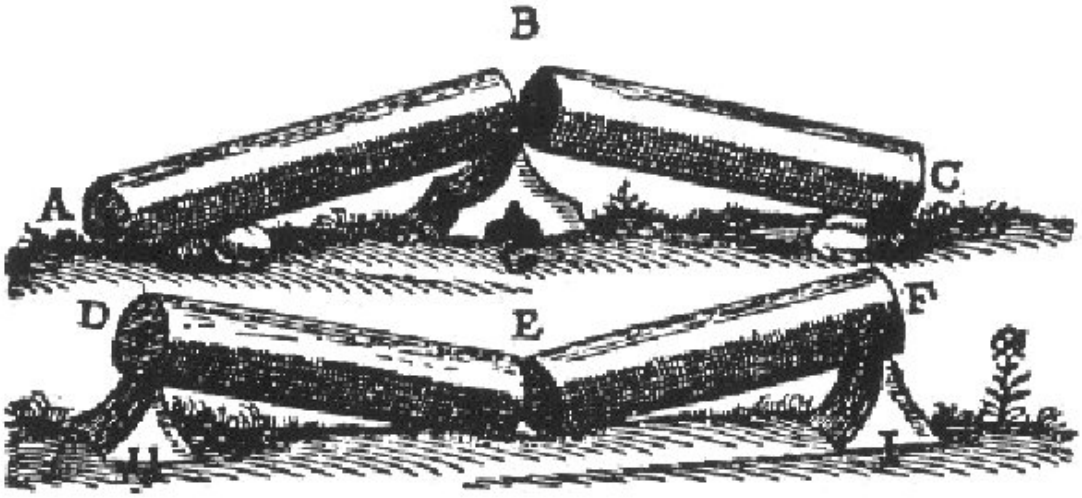

Galilei's fracture of mid-span and end-supported columns (1638).

Whereas Leonardo was concentrating on wires of different lengths but of the same thickness, Galileo Galilei (1564-1642), who is known for his contributions to mechanics, studied the strength of wires of constant length and various thicknesses. In addition to this, he also studied fracture of mid-span supported and end-supported marble columns in bending as well as fracture of marble columns loaded in axial tension (!) (Galileo Galilei, 1638). Galilei investigated also the influence of size in fracture of structures to answer the question "why do bodies break". Galileo, visiting the Venetian Arsenal, was surprised at the greater attention made by workers in construction of big ships than in small ships. He concluded that the strength of the columns depended only on the cross-sectional area and not on the length. His quasi-analytical approach led to ideas concerning

dimensional similitude which, particularly in the 19th century, dominated in the development of subsequent engineering design criteria. An account of early Italian contributions to ideas on fracture is given by R.L. Colombo and D. Firrao in this AV. Coulomb (1776) pioneered investigation of the fracture of stones in compression and nowadays his criterion is still used.

The original concept of fracture energy was conceived by Alan Arnold Griffith (1920), a British aeronautical engineer working at the Royal Aircraft Establishment (RAE) in Farnborough, where he was a senior scientific officer at the Physics Department, when he investigated the fracture of glass sheets. His great contribution to ideas about breaking strength of materials was that the weakening of material by a crack could be treated as an equilibrium problem in which the reduction in strain energy of a body containing a crack, when the crack propagates, could be equated to the increase in surface energy due to the increase in surface area. The Griffith theory began from the hypothesis that brittle material contains on elliptical microcrack, which introduces high stress concentration near the tip.

The Griffith theory predicted that the compressive strength of a material is 8 times greater than its tensile strength, but this condition can not be valid for any material. Later, the introduction of the line-crack by Irwin (1957) – a flat crack which presents two singularities at the extremes – seems to be more suitable than Griffith's crack to consider the friction which develops between crack surfaces. In 1957, George Rankine Irwin, professor of Mechanical Engineering at Lehigh University and also employed at the US Navy Research Laboratory, provided the extension of the Griffith theory to an arbitrary crack and proposed the criterion for a growth that the strain energy release rate (G) must be larger than the critical work (G_c), which is required to create a unit-crack area. Some say that notation G comes after Griffith, while others say it is after George. Furthermore, Irwin showed, using Westergaard's method, that the stress field in the area of the crack tip is completely determined by the quantity K (after Kies, a colleague of Irwin, 1952-1954), called the stress intensity factor. In the early sixties the first applications of Griffith's model to stone and concrete materials appeared place. McClintock and Walsh (1962) introduced the friction between

crack faces, whereas Kaplan (1961) focused on the possibility of applying linear elastic fracture mechanics (LEFM) to concrete. Important research about rock was carried out by Bieniawski (1965), in South Africa, where mine failures were an urgent problem to be solved.

In the same period first journals about fracture were printed (International Journal of Fracture Mechanics in 1964, Engineering Fracture Mechanics in 1970) and a treatise, edited by Liebowitz, appeared in 1968. Concerning further theoretical fracture mechanics developments, whereby the next step was the application to concrete of parameters successfully used for metals, a new parameter for fracture was provided by J. R. Rice (1968), the so-called J-integral. It was shown that in LEFM the J-integral is equivalent to the energy release rate (G). However the J-approach doesn't give correct results for concrete or concrete-like materials because of the unloading curve characterizing brittle materials and the poorly defined position of the crack tip (Hillerborg, 1983). The debate about these problems was heated further even in the 80ies.

Barenblatt (1959) and Dugdale (1960) made the first attempt at including the cohesive forces in the crack tip region within the limits of elasticity theory. Barenblatt assumed that cohesive forces acted in a small zone (the so-called cohesive zone) near the crack ends such that the faces closed smoothly. The distribution of these forces is generally unknown. For Dugdale's model, the distribution of the closing forces is known and constant according to an elastic-perfectly plastic material. However these models represent a limit as regards Hillerborg's model, which differs from both in several important aspects. It includes the tension softening process zone through a fictitious crack (without complete separation of its faces) ahead of the pre-existing crack whose lips are acted upon by such closing forces that there is no stress concentration at the tip of this extended crack. In Hillerborg's model, crack it is possible to distinguish two zones of a real crack of no more stresses transfer and a damaged zone extended in the fracture process zone (FPZ). The research began when he was professor in Building Materials at Lund Institute of Technology (Sweden) in the mid seventies. His model was suitable for concrete elements of usual size to which LEFM couldn't be applied. When the first RILEM (International Union of Testing and Research Laboratories for

Materials and Structures) technical committee on FM of concrete was formed in 1979, with Professor F.H. Wittman as chairman, Hillerborg was one of the members. In 1985 he proposed a three-point beam test to determine the fracture energy (G_f) of concrete now accepted as RILEM recommendation. G_F represents, with the tensile strength f_t and the softening law, the energy necessary to create a unit crack surface. Bazant (1984) and Bazan and Cedolin (1991) used a smeared crack model to model cracking in concrete. The crack front is assumed to consist of a diffuse zone of microcracks and the stresses, that close the FPZ faces, are represented through a stress-strain softening law. The size of this zone is related to the maximum aggregate size. An energy criterion is used for crack propagation, which can be generalized for non-linear materials behaviour. This model is particularly suitable for finite element analysis.

After Galileo, Leicester (1973) seems the first to investigate the effect of size on the strength of structures made of metals, timber and concrete. In order to illustrate the size dependence in a simple and dimensionless way, Hillerborg (1976) introduced the concept of a characteristic length.

Carpinteri (1980) proposed a parameter $s=K_{IC}/\sigma_y h^{1/2}$ of concrete as a measure of structural brittleness, but later (1986) introduced the energy brittleness number (or Carpinteri-number) $S_e= G_F/f_t h$, where h is the characteristic length. Bazant's size effect Law (1984) gives a measure of the brittleness of concrete. According to this law, the size effect is transitional between the yield limit and the LEFM size effect.

Reasons for fracture mechanics in concrete

Bazant pointed out five reasons for the necessity of introducing fracture mechanics into the design of structures among which the size effect is the most compelling. The application of FM is most urgent for such structures as concrete dams and nuclear vessels or containments, for which the safety concerns are particularly high and the consequences of a potential disaster could be enormous. Since concrete structures have been designed and successfully built according to codes which

totally ignore fracture mechanics theory, it might seem unnecessary to change the current practice. Nevertheless, there are five compelling reasons for doing so.

Reason 1: Energy required for crack formation

From the strictly physical viewpoint, although crack initiation may depend on stress, the actual formation of crack requires a certain amount of energy.

Reason 2: Objectivity of calculation

Any physical theories must be objective in the sense that the result of calculations must not depend on subjective aspects such as the choice of coordinates, and the choice of mesh, etc. If a theory is found to be unobjective, it must be rejected. There is no need to even compare it to experiments. Objectivity comes ahead of experimental verification.

A powerful approach in the finite element analysis is the concept of smeared cracking, introduced by Rashid (1968). After strain-softening had been implemented in finite element programs and widely applied, it was discovered that the convergence properties were incorrect and the calculation results were not objective with regard to the analyst's choice of the mesh, i.e., the results significantly change if the mesh was refined (Bazant and Belytschko, 1984). By specifying the energy dissipated by cracking per unit length of the crack or the crack band, the overall energy dissipation is forced to be independent of the element subdivision.

Reason 3: Nonexistence of yield plateau

Based on stress-strain diagrams or load-deflection diagrams, one may distinguish two basic types of structural failure: plastic and brittle. The present code-sanctioned design approach, that is the plastic-limit analysis, is valid only if there is a prolonged yield plateau, both in the stress-strain and load-deflection diagrams. But yield plateaus are seen neither in the stress-strain tests of concrete nor in the load-deflection diagrams observed in the brittle types of failures in concrete structures. Hence, considering failure propagation is inevitable.

Reason 4: Energy absorption capability and ductility

The area under the entire load-deflection diagram represents the energy which the structure

could absorb during failure and must therefore be supplied by the loads. Consideration of this energy is important especially for dynamic loading, and determines the ductility of the structure. Plastic limit analysis can't give any information about the post-peak decline of the load-deflection curve. This can't be accomplished without fracture mechanics.

Reason 5: Size effect

The size effect is probably the most compelling reason for using fracture mechanics, and is conveniently characterized in terms of the normal stress at maximum (ultimate) load. When the normal stresses in geometrically similar structures of different sizes are identical, it can say that there is no size effect.

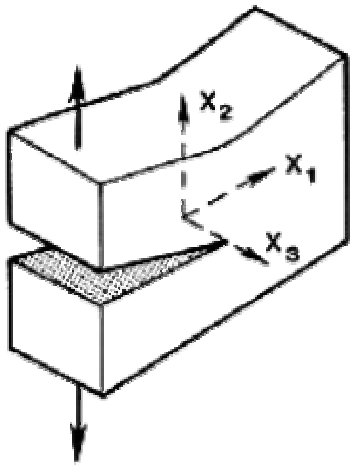

Mode I
(Opening Mode)

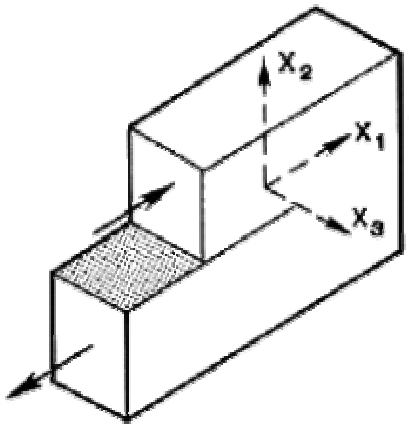

Mode II
(Sliding Mode)

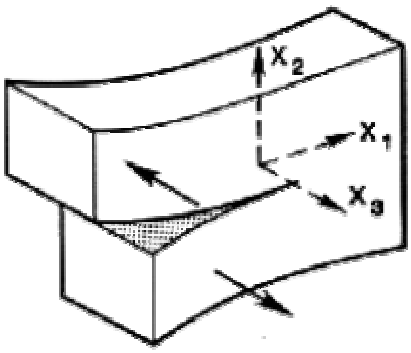

Mode III
(Tearing Mode)

Figure 2.1 Fundamental fracture mode I, mode II and mode III.

Another size effect which calls for the use of fracture mechanics is the effect of size on ductility. Ductility of a structure may be characterized by the deformation at which the structure fails under a given type of loading. For loading in which the load is controlled, structures fail at their maximum load, while structural elements that are loaded under displacement control or through displacement-controlled elastic devices fail in their post-peak (strain-softening) range. A decrease in ductility of a structure represents an increase in its brittleness.

Linear elastic fracture mechanics (LEFM)

In LEFM, it is assumed that all of the fracture process happens at the crack tip and that the entire volume of the body remains elastic. Under this assumption, crack propagation and structural failure can be solved. It is convenient to distinguish three elementary fracture modes, mode I, mode II and mode III, also called the opening mode, the shearing or sliding mode and the tearing mode as shown in Figure 2.1. Mode I and mode II are planar symmetric and anti-symmetric, while mode III is three-dimensional. General fracture is a linear combination of these three modes.

Introduction of a crack into a linear elastic body produces stress concentrations near the crack tips. The stress field is singular at the crack tip, with all the nonzero stress components approaching infinity as the radial distance r from the crack tip tends to zero. Consider a through-thickness crack of arbitrary size, a, in a body of arbitrary size and shape loaded by arbitrary mode I loading.

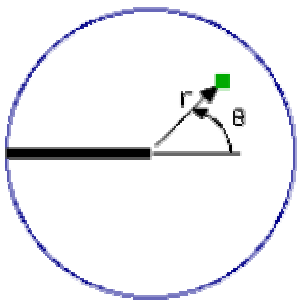

The in-plane crack tip stresses can be expressed by $\sigma_{ij} = \frac{K_I}{\sqrt{2\pi r}} f_{ij}(\theta)$.

Where, K_I = the stress intensity factor of mode I. For example, $K_I = \sigma\sqrt{\pi a}$ for an infinite plate (with a central crack 2*a*) subjected to uniform tension σ. It is noted that K_I is a function of loading and geometry. The crack propagates when $K_I = K_{IC}$, where K_{IC} is the fracture toughness.

A material is considered to be notch sensitive if the presence of a notch causes a change in the net section strength (σ_{net}) of the material. σ_{net} is calculated on the basis of the reduced cross-section but neglecting the stress concentration effect of the notch. This means that the measured fracture toughness of concrete K_{IC} should be constant for a notch sensitive material. Notch sensitivity is a necessary but not sufficient condition for the applicability of LEFM. Kesler et al. (1972) concluded that the concept of LEFM is not directly applicable to cement paste, mortar and concrete. However, a reanalysis of their data by Saouma et al. (1980), using modern computational techniques, suggested that their conclusions regarding hardened cement paste are open to question, and showed that a single parameter K_{IC} approach to crack propagation can be used within engineering accuracy. Shah and McGarry (1971) studied the notch sensitivity in mortar and concrete and concluded that they are notch insensitive when the crack length is shorter than a few centimeters. A number of other investigations have also shown that mortar and concrete are notch insensitive for notch lengths up to at least 50mm. On the other hand, some other studies have shown that mortar and concrete is notch sensitive though to a lesser degree than cement.

Some of these contradictions were explained in terms of specimen size. Walsh (1976) has argued that for concrete, flexural specimens would appear to be notch insensitive and hence cause a variation in the measured values of K_{IC} if they are too small, and he suggested a minimum beam depth of about 230mm. Carpinteri (1982), from his definition of the brittleness number *s*, concluded that for a concrete beam to be notch sensitive a minimum specimen depth of about 60mm would be required. Modeer (1979), using the fictitious crack model, computed the minimum beam depth as

2-3m. Bazant (1980) has suggested that the minimum beam depth should be least 100 times the size of the microcracked region, or about 500 times the maximum aggregate size. For 20mm aggregate, this would lead to a minimum depth of 10 m. In this procedure which was suggested by Jenq and Shah (1985), acoustic emission (AE) measurement was available to detect the load level at which unstable crack growth took place. Swartz and co-workers (1984) explained the variation in the measured (K_{IC}) values by Walsh (1976) and Nasu and Lott (1969), noting that their data were referenced to the original notch depth. This violates one of the requirements of ASTM methods for metals, namely that a true crack is not a notch to be used.

Fracture process zone (FPZ) and fracture parameters

The propagation of a crack in concrete involves a great deal of microcracking, much of it occurring in the highly stressed region ahead of the apparent crack tip. According to Bazant and Oh (1983), the fracture process zone represents the nonlinear zone ahead of the crack tip in which the material undergoes progressive microcracking, and is manifested by strain softening behavior. On the other hand, Shah (1988 and 1991) has equated the fracture process zone as the region of precritical crack growth (or slow crack growth) which precedes the maximum load. Thus, while there is general agreement that a fracture process zone exits in cementitious materials, there is no agreement on exactly what constitutes a process zone in concrete. Mindess (1991) stressed the importance of quantifying the extent of the damage that occurs during fracture of concrete by defining the fracture process zone as the region of discontinuous microcracking ahead of the continuous (visible) crack.

A necessary condition for the applicability of LEFM is that the fracture process zone should be small compared to the structure's dimensions. Mindess (1991) compiled the results obtained by all available experimental techniques for measuring the size of FPZ. He concluded that FPZ is not a fundamental material property (at least for laboratory size specimens), but depends on the specimens and the methods of loading. He also reported that the estimated size of FPZ ranges

from only a few mm up to perhaps 500mm. To complicate things further, in their investigation of mode I fracture in compact tension (CT) specimens using a scanning electron microscope (SEM) system, Diamond and Bentur (1985) observed that there is no straight main crack, and the full length of the crack is tortuous, frequently branched, and almost irregular. In nonlinear fracture mechanics modeling, it is often implied that the main crack is assumed to be straight and unbranched, and FPZ exists ahead of the visible crack tip. Furthermore, Swartz (1986) conducted an extensive testing program for beams under bending with static and fatigue precracking as well as load control. He concluded that LEFM is suitable to describe cracking and fracture in concrete if slow crack growth is considered. He confirmed his conclusions by using a dye technique which revealed the existence of a very small process zone ahead of the crack front, independent of the crack length or beam depth. Yon et al. (1992) investigated dynamic fracture of three-pint bending specimens and found out that FPZ does not fully develop in the specimens subjected to slow strain rate loading ($<1.74 \times 10^{-2} sec^{-1}$) and recommended beams with larger depths for comprehensive studies of strain rate effects on FPZ.

It must also be noted that the length of FPZ for mixed-mode fracture differs from that of mode I fracture. For mixed-mode fracture, contradictory results have been reported. Carpinteri and Swartz (1991) reported that with a mixed-mode crack configuration, larger (specimen and crack) sizes are needed than with a model I crack configuration, in order to utilize LEFM correctly. This implies that the fracture process zone is longer for the mixed-mode configuration. The opposite conclusion was reported by Castro-Montero et al. (1992) in their experimental investigation of mode I and mixed-mode fracture using disk specimens. They concluded that the size of the fracture process zone depends on the mode of fracture. The size of FPZ in mixed-mode was smaller than in mode I for short crack lengths. For longer crack lengths, after the crack has taken a straight line trajectory, FPZ in mixed-mode approaches the planar dimension of FPZ in mode I. Horii (1991) stated that LEFM cannot be applied for pure mode I where the bridging stress across the crack surface plays an important role, i.e. FPZ is of an appreciable size.

A summary of the values of the fracture parameters measured and the experimental techniques till the year 1984 is given by Mindess (1984). The summarized fracture parameters are the fracture energy (G_f), fracture toughness (K_{IC}), and critical strain energy release rate (G_{IC}) for mode I fracture. The fracture energy was introduced in fictitious crack model (FCM) as a material parameter by Hillerborg (1976). Fracture toughness of concrete is defined as the critical stress intensity factor K_{IC} of LEFM, and G_{IC} is the corresponding strain energy release rate. The summarized results revealed that K_{IC} increased with aggregate volume, with increasing size of the coarse aggregate, and with increasing roughness of the aggregate. K_{IC} also increased with age and showed a tendency to increase slightly with the increase in the rate of loading. K_{IC} decreased with increasing W/C ratio, and with increasing air content. However, the results concerning the dependency of K_{IC} values on the crack length were quite contradictory. The results also showed an increase of K_{IC} with specimen size, and a variation of K_{IC} with test geometry. Mindess (1984) pointed out that, apart from the problem of the size effect, the cause of these discrepancies could be inherent in the experimental techniques themselves.

Based on the work of Hillerborg (1985) and other researcher - RILEM (1985) proposed a standard test for measuring the fracture energy (G_f) the method uses a beam specimen loaded in three-point bending with a central edge notch. Several works have done to show the influence of concrete mechanical parameters on the value of G_f. Petersson (1981) obtained the following results: G_f decreases when W/C increases; G_f seems to increase somewhat with increasing volume fraction of aggregate; G_f seems to be insensitive to size of aggregate (d_a); stronger aggregates produce a higher value of G_f than that produced by weaker aggregates. In a compilation of the results obtained from testing 700 beams according to RILEM proposal, Hillerborg (1985) concluded that there was no major influence of W/C but there was a tendency for G_f to increase with d_a increasing from 8mm to 20mm. Wittmann et al. (1987) concluded that larger specimens, higher rate of loading, larger d_a and smaller W/C give large values to G_f. Hordijk et al. (1989) revealed that G_f depends on the maximum aggregate size, W/C ratio, age of loading, curing conditions, temperature, loading rate,

and specimen dimensions. They found out that G_f grows with both increasing maximum aggregate size and fracture ligament length of the specimen. However, values of G_f independent of specimen dimension, i.e. fracture ligament length, were obtained from specimens with ligament lengths longer than 300mm.

Another important fracture characteristic of the FCM is the tension softening curve. It was shown by Petersson (1981) and also by Roeflstra and Wittmann (1986) that the response of a notched beam can vary when the analysis is done with constant G_f but with varying the shape of the tension softening curve. The most direct way to determine the relation for concrete under tensile loading is by means of a uniaxial tensile test under deformation control. In the test, a uniform stress field should be applied to the cracking plane and the stress field should stay uniform during the fracture process. Because the localization of fracture takes place in a small zone, arrangements have to be made to ensure that the crack propagates inside the measurement zone. An overview of different uniaxial tensile tests is given by Hordijk (1989). A disadvantage of the uniaxial tensile test is the difficulty to perform it in a stable manner. It can only be performed with sophisticated equipment and is therefore not suitable as a standard test. A different approach is to determine the softening relation by inverse modeling. In this approach, as proposed by Wittmann (1986), an experiment is simulated by means of a number of finite element calculations and the relation giving the best fit is regarded to be the material property.

A new method for performing stable uniaxial tests has been proposed by Carpinteri and Ferro (1993) to determine the tensile strength and the fracture energy. However, even in their method, it is doubtful that uniform opening takes place in the zone of measurement as demonstrated by van Mier et al., (1993). A correction for the RILEM three-point bending test was also proposed by other researchers to derive the fracture energy without the effects of experimental procedures, bulk energy dissipation, and size effects. However, it is not evident yet that this method is valid for different types of experiments.

The applicability of FCM to analyze mode I fracture relies significantly on the material

functions and parameters involved in the model. Several researchers showed that the results obtained by FCM are very sensitive to the values of Young's modulus (Ec), tensile strength (f_t), fracture energy (G_f), and the shape of the tensile softening curve.

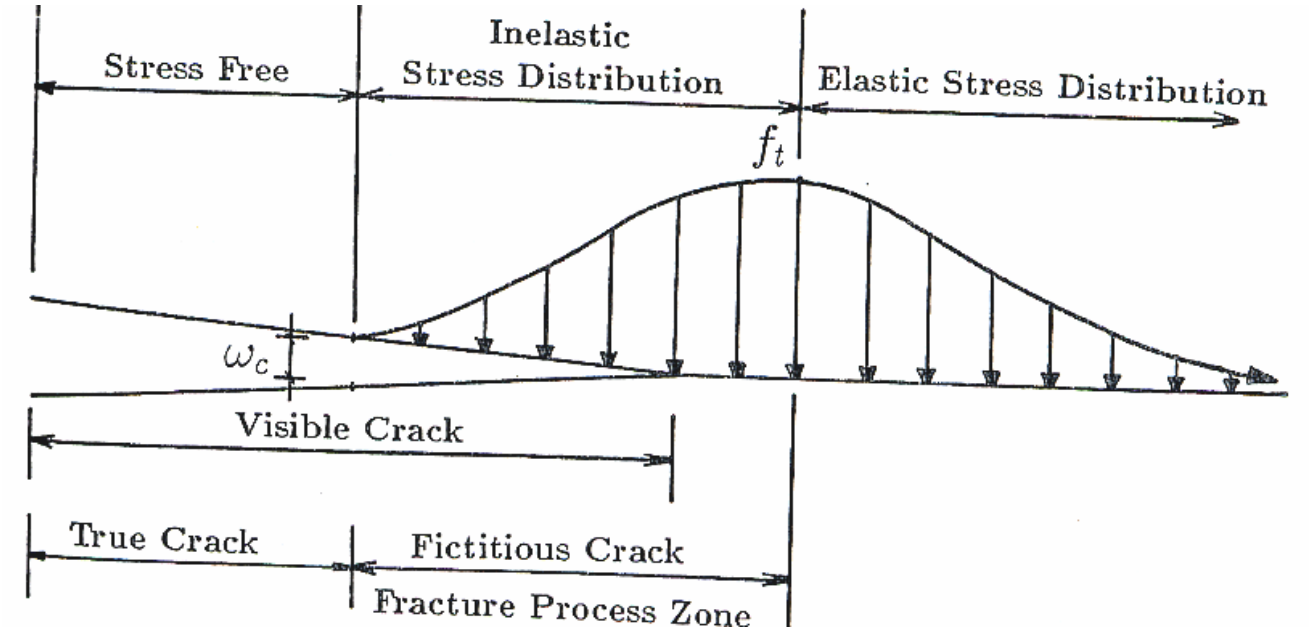

Figure 2.2 Stress distribution near the crack tip for FCM.

A typical crack tip stress distribution as shown in Figure 2.2 based on the proposed FCM. FPZ is modeled as an extension of the actual crack subjected to a closing stress which depends on the crack opening displacement.

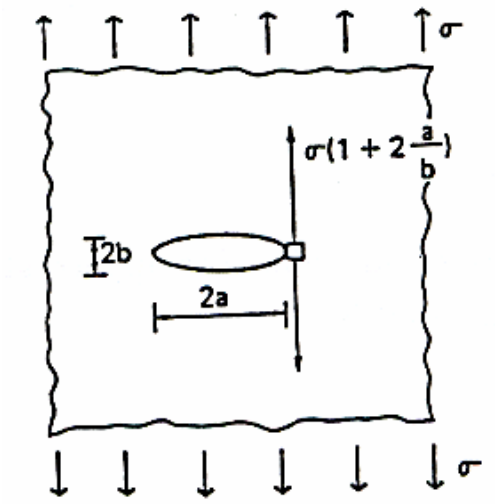

Figure 2.3 Stress concentration at the edge of an elliptical cavity.

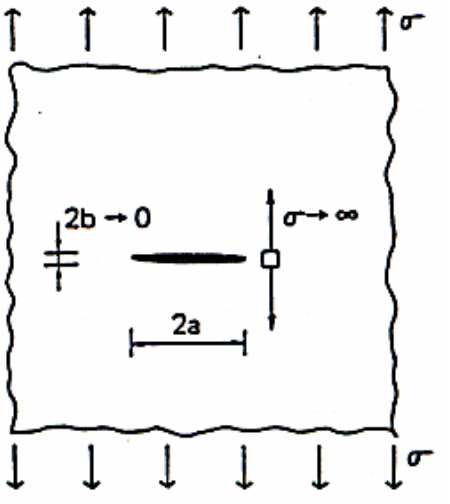

Figure 2.4 Limit-case of a highly prolated elliptical cavity.

Mixed-mode crack propagation

The applicability of fracture mechanics principles to analyze crack initiation and propagation in concrete under tensile mode I loading has encouraged researchers to try applying them to mixed-mode fracture investigation. In concrete structures, cracks propagate under the combined action of both tensile (mode I) and shear (mode II) fracture. The influence of mode II fracture on the process of cracking in concrete structures is of great practical importance. In theoretical treatment, the mixed-mode crack propagation is a complicated problem to predict crack trajectory and crack instability. In this regard, implementation of FCM in the analysis of mixed-mode fracture problems suffers from the limitation associated with modeling FPZ. There is still no general theory for the description of cohesive crack evolution with normal and tangential cohesive stresses. Accordingly, the development of another numerical technique for mixed-mode cracking analysis is necessary for the practical application of fracture mechanics to concrete structures. Consequently, basic theories are reviewed and discussed.

Griffith's model

Inglis (1913) provided the solution for a solid weakened by an elliptical cavity subjected to a uniform stress σ normal to the major semi-axis of the ellipse, as shown in Figure 2.3. The maximum normal stress at the immediate vicinity y=0 and x $\rightarrow$0 is given by,

$$\sigma_{\max} = \sigma\left(1 + 2\frac{a}{b}\right) = \sigma\left(1 + 2\sqrt{\frac{a}{\rho}}\right) \approx 2\sigma\sqrt{\frac{a}{\rho}} \qquad 2.1$$

Where a and b are the major and minor semi-axes of the ellipse, respectively, and $\rho=b^2/a$ is the radius of curvature at the end of the major axis. The strength of the solid depends only on the ratio of the semi-axes of the ellipse. The stress concentration factor (1+2a/b) increases with the increase of the ellipse elongation. When a/b$\rightarrow\infty$, i.e. when the ellipse is very prolate as shown in Figure 2.4, the stress concentration factor tends to infinity. Therefore, such a model does not appear to be useful

for describing the critical condition for a notch of length 2a and vanishing width 2b.

Griffith (1920) extended Inglis' work. Griffith thought again about the infinite plate under tension, but he stretched the ellipse out into a crack. Griffith proved that the elastic energy W_e released by a uniformly stretched plate of unite thickness, when the latter is cut by a crack of length 2a as shown in Figure 2.5, is proportional to the energy contained in the circle of radius a prior to cutting. Griffith showed that,

$$W_e = \pi a^2 \frac{\sigma^2}{E}, \qquad 2.2$$

where E is the Young's modulus of the material.

On the other hand, the surface energy required to create a crack of length 2a is

$$W_s = 4a\gamma = 2aG_{IC}, \qquad 2.3$$

where γ is the unit surface energy, and $G_{IC} = 2\gamma$ is the critical strain energy release rate.

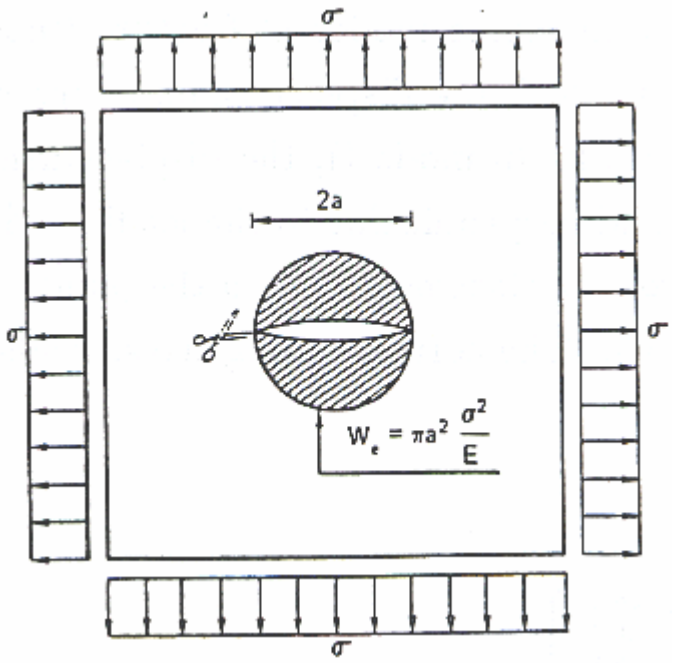

Figure 2.5 Griffith's crack in an infinite slab subjected to a uniform stress field.

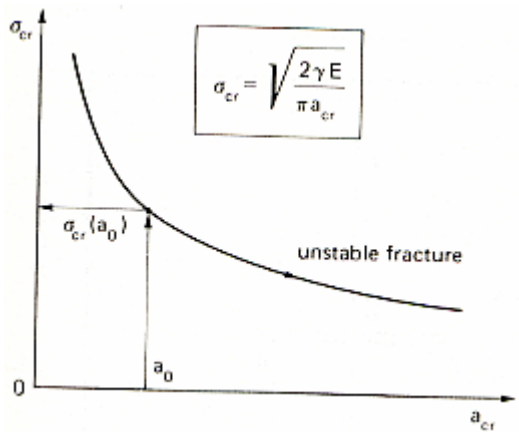

Figure 2.6 Stress of crack propagation versus crack half-length.

Griffith assumed that a pre-existing crack of length 2a can propagate when the elastic energy released during the crack extension is equal to or larger than the surface energy required for creating the newly formed crack surface, that is when,

$$\frac{dW_e}{da} \geq \frac{dW_s}{da}, \qquad 2.4$$

which leads to,

$$\sigma \geq \sqrt{\frac{EG_{IC}}{\pi a}}, \qquad 2.5$$

The instability condition for crack growth occurs when the applied stress σ reaches the critical value σ_{cr} for the crack length $2a_{cr}$, that is

$$\sigma_{cr} = \sqrt{\frac{EG_{IC}}{\pi a}}. \qquad 2.6$$

Figure 2.6 gives the variation of the crack propagation stress σ with the semi-length a of the crack, i.e. a plot of Eq.2.6. As the critical crack semi-length a_{cr} tends to increase, the critical fracture stress σ_{cr} decreases, and the fracture process results to be unstable. The pair of values σ

and a under the curve represent stable cases, whereas pairs above it signify unstable cases.

Irwin's model

Irwin (1957) reconsidered the cracked plate subjected to a uniform stress shown in Figure 2.7, where (r, θ) denotes the local polar coordinates. He recognized that the Griffith strain energy release rate G can be described in terms of a parameter which characterizes the state of stress or strain in the region around the crack tip. This parameter K, called the stress intensity factor, is related to the strain energy release rate as follow:

$G = K^2 / E$ (for plane stress) 2.7

$G = (1-\nu^2)K^2 / E$ (for plane strain),

where ν is the Poisson's ratio of the material.

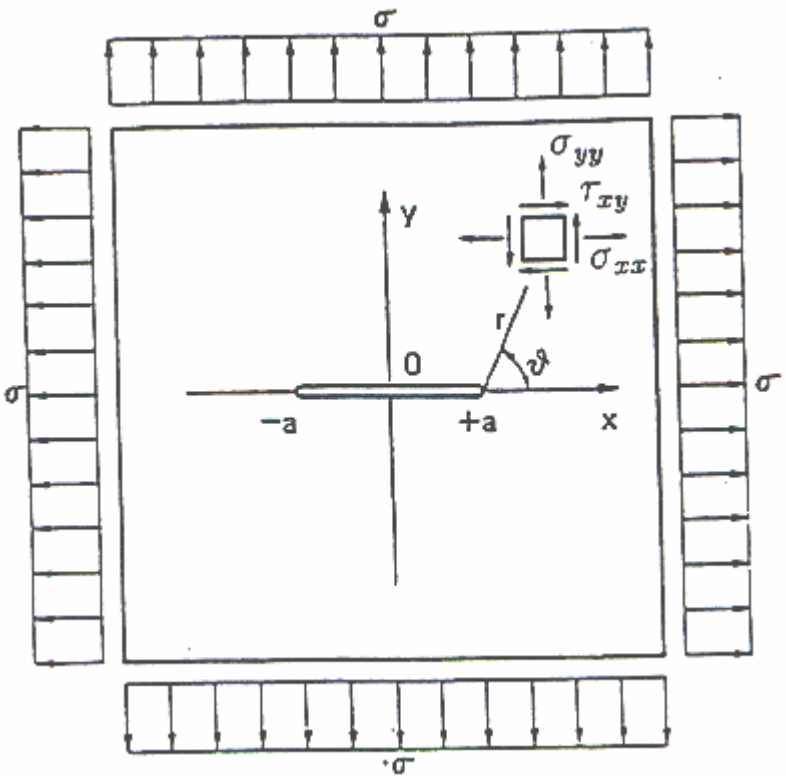

Figure 2.7 Stress notation in the crack tip vicinity in Irwin's model.

Irwin also proposed a mathematical model which expresses the stress fields near the crack tip in terms of stress intensity factors for the three modes of fracture (mode I, mode II and mode III as shown in Figure 2.1). In mode I, the displacements of the crack surfaces are perpendicular to the plane of the crack. In mode II, the displacements of the crack surfaces are in the plane of the crack and perpendicular to the leading edge of the crack. For mode III fracture, the crack surface displacements are in the plane of the crack and parallel to the leading edge of the crack. The corresponding stress fields and are given, as follows, with the reference to Fig.2.8.

Mode I fracture

$$\sigma_{xx} = \frac{K_I}{\sqrt{2\pi r}} \cos\frac{\theta}{2}\left(1 - \sin\frac{\theta}{2}\sin\frac{3\theta}{2}\right) \qquad 2.8$$

$$\sigma_{yy} = \frac{K_I}{\sqrt{2\pi r}} \cos\frac{\theta}{2}\left(1 + \sin\frac{\theta}{2}\sin\frac{3\theta}{2}\right) \qquad 2.9$$

$$\tau_{xy} = \frac{K_I}{\sqrt{2\pi r}} \cos\frac{\theta}{2}\sin\frac{\theta}{2}\cos\frac{3\theta}{2} \qquad 2.10$$

$$u = \frac{K_I}{2\mu}\sqrt{\frac{r}{2\pi}}\left[\cos\theta\left(\kappa - 1 + 2\sin^2\frac{\theta}{2}\right)\right] \qquad 2.11$$

$$v = \frac{K_I}{2\mu}\sqrt{\frac{r}{2\pi}}\left[\sin\frac{\theta}{2}\left(\kappa + 1 - 2\cos^2\frac{\theta}{2}\right)\right] \qquad 2.12$$

Mode II fracture

$$\sigma_{xx} = -\frac{K_{II}}{\sqrt{2\pi r}} \sin\frac{\theta}{2}\left(2 + \cos\frac{\theta}{2}\cos\frac{3\theta}{2}\right) \qquad 2.13$$

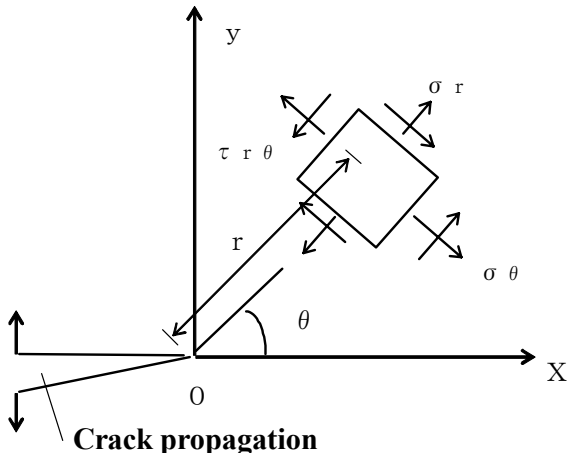

Figure 2.8 Stress notation in the crack tip vicinity.

$$\sigma_{yy} = \frac{K_{II}}{\sqrt{2\pi r}}\left(\sin\frac{\theta}{2}\cos\frac{\theta}{2}\cos\frac{3\theta}{2}\right) \qquad 2.14$$

$$\tau_{xy} = \frac{K_{II}}{\sqrt{2\pi r}}\cos\frac{\theta}{2}\left(1-\sin\frac{\theta}{2}\sin\frac{3\theta}{2}\right) \qquad 2.15$$

$$u = \frac{K_{II}}{2\mu}\sqrt{\frac{r}{2\pi}}\left[\sin\frac{\theta}{2}\left(\kappa+1+2\cos^2\frac{\theta}{2}\right)\right] \qquad 2.16$$

$$v = -\frac{K_{II}}{2\mu}\sqrt{\frac{r}{2\pi}}\left[\cos\frac{\theta}{2}\left(\kappa-1-2\sin^2\frac{\theta}{2}\right)\right] \qquad 2.17$$

Mode III fracture

$$\tau_{xz} = \frac{K_{III}}{\sqrt{2\pi r}}\left(-\sin\frac{\theta}{2}\right) \qquad 2.18$$

$$\tau_{yz} = \frac{K_{III}}{\sqrt{2\pi r}}\left(\cos\frac{\theta}{2}\right) \qquad 2.19$$

$$w = \frac{2K_{III}}{\mu}\sqrt{\frac{r}{2\pi}}\left[\sin\frac{\theta}{2}\right] \qquad 2.20$$

Where μ=E/2(1+ν) is the shear modulus, for plane stress, $\kappa = (3-\nu)/(1+\nu)$, for plane strain, $\kappa = (3-4\nu)$. K_I, K_{II}, and K_{III} are known as the mode I, mode II, and mode III stress intensity factors, respectively.

For the Griffith's crack (as shown in Figure 2.4), the model I stress intensity factor is given by,

$$K_I = \sigma\sqrt{\pi a}. \qquad 2.21$$

It is important to note that the stress intensity factor has the unit of $[stress]\sqrt{length} = [F]\,[L]^{-3/2}$.

Since the stress field in the vicinity of the crack tip is uniquely defined by the K_I factor, it is consistent to assume the instability to occur when K_I achieves its critical value K_{IC}, that is to say,

$$\sigma_{cr} = \frac{K_{IC}}{\sqrt{\pi a_{cr}}}. \qquad 2.22$$

Comparing Eqs.2.6 and 2.22, the LEFM relationship between the critical stress intensity factor K_{IC}, which represents a measure of the fracture toughness of the material, and the critical strain energy release rate G_{IC} for the plane state is,

$$K_{IC} = \sqrt{EG_{IC}}, \qquad 2.23$$

and for the plane strain state,

$$K_{IC} = \sqrt{\frac{EG_{IC}}{1-\nu^2}}. \qquad 2.24$$

In LEFM, the fracture energy G_f is equal to the energy dissipated in the unit surface $G_{IC}=2\gamma$, therefore the fracture toughness K_{IC} can be related to the fracture energy G_f as follows:

For plane stress $K_{IC} = \sqrt{EG_f}$ 2.25

For plane strain $K_{IC} = \sqrt{\frac{EG_f}{1-\nu^2}}.$ 2.26

Principles of mixed-mode fracture

The linear elastic fracture mechanics analysis idealizes the physical crack problem in the following three principles:

1. The crack plane is generally taken to be flat.
2. The crack is assumed to be so sufficiently large that local material microstructure can be modeled as a continuum.
3. Inelastic crack-tip effect as plasticity is restricted to small volume so that they may be neglected.

For a traction-free crack in an infinite domain, the two-dimensional stress fields at the point (r,θ) in the general case of mixed-mode fracture are obtained by adding the equations from mode I and mode II fracture.

$$\sigma_{xx} = \frac{K_{\mathrm{I}}}{\sqrt{2\pi r}}\cos\frac{\theta}{2}\left(1-\sin\frac{\theta}{2}\sin\frac{3\theta}{2}\right) - \frac{K_{\mathrm{II}}}{\sqrt{2\pi r}}\sin\frac{\theta}{2}\left(2+\cos\frac{\theta}{2}\cos\frac{3\theta}{2}\right) \qquad 2.27$$

$$\sigma_{yy} = \frac{K_{\mathrm{I}}}{\sqrt{2\pi r}}\cos\frac{\theta}{2}\left(1+\sin\frac{\theta}{2}\sin\frac{3\theta}{2}\right) + \frac{K_{\mathrm{II}}}{\sqrt{2\pi r}}\sin\frac{\theta}{2}\cos\frac{\theta}{2}\cos\frac{3\theta}{2} \qquad 2.28$$

$$\tau_{xy} = \frac{K_I}{\sqrt{2\pi r}}\cos\frac{\theta}{2}\sin\frac{\theta}{2}\cos\frac{3\theta}{2} + \frac{K_{II}}{\sqrt{2\pi r}}\cos\frac{\theta}{2}\left(1-\sin\frac{\theta}{2}\sin\frac{3\theta}{2}\right) \quad 2.29$$

$$u = \frac{K_I}{4\mu}\sqrt{\frac{r}{2\pi}}\left[(2\kappa-1)\cos\frac{\theta}{2}-\cos\frac{3\theta}{2}\right] + \frac{K_{II}}{4\mu}\sqrt{\frac{r}{2\pi}}\left[(2\kappa+3)\sin\frac{\theta}{2}+\sin\frac{3\theta}{2}\right] \quad 2.30$$

$$v = \frac{K_I}{4\mu}\sqrt{\frac{r}{2\pi}}\left[(2\kappa+1)\sin\frac{\theta}{2}-\sin\frac{3\theta}{2}\right] - \frac{K_{II}}{4\mu}\sqrt{\frac{r}{2\pi}}\left[(2\kappa-3)\cos\frac{\theta}{2}+\cos\frac{3\theta}{2}\right] \quad 2.31$$

In the two-dimensional mixed-mode problems, stresses are conveniently expressed in the polar (r, θ) coordinates as σ_r, σ_θ, and $\sigma_{\theta\tau}$, . The origin of coordinates is taken at the crack tip and θ=0 corresponds to the crack line as shown in Figure 2.9. Eqs.2.27, 2.28 and 2.29 can now be written in polar coordinates as follows,

$$\sigma_r = \frac{1}{\sqrt{2\pi r}}\cos\frac{\theta}{2}\left[K_I\left(1+\sin^2\frac{\theta}{2}\right) + K_{II}\left(\frac{3}{2}\sin\theta - 2\tan\frac{\theta}{2}\right)\right] \quad 2.32$$

$$\sigma_\theta = \frac{1}{\sqrt{2\pi r}}\cos\frac{\theta}{2}\left[K_I\cos^2\frac{\theta}{2} - \frac{3}{2}K_{II}\sin\theta\right] \quad 2.33$$

$$\tau_{r\theta} = \frac{1}{2\sqrt{2\pi r}}\cos\frac{\theta}{2}\left[K_I\sin\theta + K_{II}(3\cos\theta - 1)\right] \quad 2.34$$

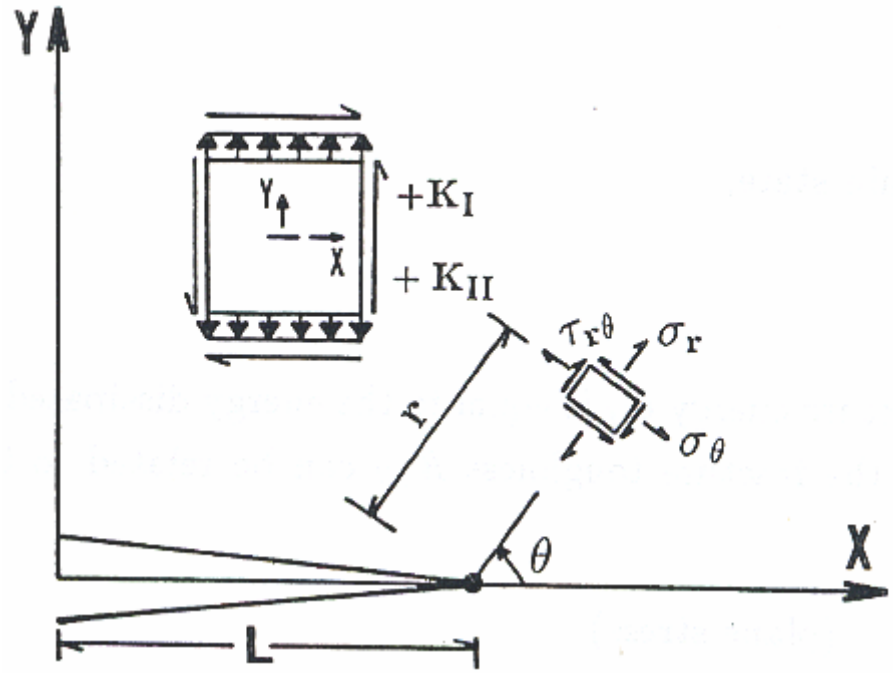

Figure 2.9 State of stress near the crack tip in polar coordinates (r,θ).

The following four criteria for crack initiation are proposed.

(1) Maximum tangential stress criterion "$\sigma_{\theta max}$"

The crack extension starts in the radial direction, perpendicular to the direction of the maximum tension, i.e., corresponding to $\sigma_{\theta max}$ and $\tau_{r\theta}=0$. Here, θ is obtained by solving the following equation:

$$K_I \sin\theta + K_{II}(3\cos\theta - 1) = 0 \qquad 2.35$$

and the crack propagates when,

$$\cos\frac{\theta}{2}\left[\frac{K_I}{K_{IC}}\cos^2\left(\frac{\theta}{2}\right) - \frac{3}{2}\frac{K_{II}}{K_{IC}}\sin\theta\right] \geq 1. \qquad 2.36$$

(2) Minimum strain energy density function criterion "$S_{\theta min}$"

The strain energy density function is defined as follows,

$$S(\theta) = a_{11}K_I^2 + 2a_{12}K_I K_{II} + a_{22}K_{II}^2, \qquad 2.37$$

where, $a_{11} = \dfrac{(1+\cos\theta)(\kappa-\cos\theta)}{16\mu}$,

$$a_{12} = \frac{\sin\theta[2\cos\theta-(\kappa-1)]}{16\mu},$$

$$a_{22} = \frac{(\kappa+1)(1-\cos\theta)+(1+\cos\theta)(3\cos\theta-1)}{16\mu},$$

and μ and κ are the same as defined earlier.

The crack extension takes place in the direction along which the strain energy density function possesses a minimum value, i.e. when,

$$\frac{dS}{d\theta} = 0 \qquad \text{and} \qquad \frac{d^2S}{d\theta^2} > 0. \qquad 2.38$$

An iterative minimization procedure is utilized to solve eqs.(2.38) and compute the values of θ and $S_{\theta min}$. The crack propagation would be initiated when $S_{\theta min}$ reaches the critical value $S_{cr} = \dfrac{(1-2\nu)(1+\nu)K_{IC}^2}{2E}$, i.e. when, $\dfrac{S_{\theta\min}}{S_{cr}} \geq 1$.

(3) Maximum tangential strain criterion "$\varepsilon_{\theta max}$"

The tangential strain ε_θ is defined as follows,

$$\varepsilon_\theta = \frac{K_I}{E\sqrt{2\pi r}}\left[\cos\frac{\theta}{2}\left(\frac{3}{4}-\frac{5}{4}\nu\right)+\frac{1}{4}\cos\frac{3\theta}{2}(1+\nu)\right] + \frac{K_{II}}{E\sqrt{2\pi r}}\left[\sin\frac{\theta}{2}\left(-\frac{3}{4}+\frac{5}{4}\nu\right)-\frac{3}{4}\sin\frac{3\theta}{2}(1+\nu)\right] \quad 2.39$$

Crack extension direction θ is determined by maximizing ε_θ through an iterative maximization procedure, and the crack propagates when $\varepsilon_{\theta max}$ reaches the critical value $\varepsilon_{cr} = \frac{K_{IC}(1-\nu)}{E\sqrt{2\pi r}}$ obtained by considering θ=0 and σ_r=0. In other words, the criterion for crack propagation is given by,

$$\frac{\varepsilon_{\theta\max}}{\varepsilon_{cr}} \geq 1. \quad 2.40$$

(4) Maximum energy release rate criterion "$G_{\theta max}$"

The crack extension occurs in the direction of the maximum energy release rate. The angle of crack propagation θ is obtained by maximization of the energy release rate function G_θ by iterations, where,

$$G_\theta = \frac{4}{E(3+\cos^2\theta)^2}\left(\frac{1-\frac{\theta}{\pi}}{1+\frac{\theta}{\pi}}\right)^{\frac{\theta}{\pi}}\left[(1+3\cos^2\theta)K_I^2 - 8\sin\theta\cos\theta K_I K_{II} + (9-5\cos^2\theta)K_{II}^2\right] \quad 2.41$$

Maximizing G_θ in eq.(2.41) is equivalent to satisfying the following condition,

$$\left.\begin{aligned} &\frac{dG}{d\theta} = 0 \\ &\text{and} \\ &\frac{d^2G}{d\theta^2} < 0. \end{aligned}\right\} \quad 2.42$$

The crack propagates when $G_{\theta max}$ exceeds the critical strain energy release rate

$G_{IC} = \frac{K_{IC}^2}{E}$, hence,

$$\frac{G_{\theta\max}}{G_{IC}} \geq 1. \quad 2.43$$

3. Application of Acoustic emission (AE) technique for Nondestructive testing (NDT)

Nondestructive testing (NDT) is defined as the technical method to examine materials or components in ways that do not impair future usefulness and serviceability. NDT can be used to detect, locate, measure, and evaluate flaws to assess integrity, properties, and composition and to measure geometric characteristics (ASTM E1316). Various NDT technologies, such as ultrasonic-based methods, radiographic methods, dynamic methods, acoustic emission (AE) technique have been studied.

This review focuses on the feasibility of the AE technique for monitoring cracks in concrete structures. It also summarizes the advantages and disadvantages of the technique.

General concepts

Acoustic emission (AE) is a phenomenon frequently encountered in everyday life. An example of AE is the sound of a pencil being broken or wood being split. Technically, AE is defined as the class of phenomena in which transient elastic waves are generated by the rapid release of energy from a localized source or sources within a material (ASTM E1316).

AE occurs in a range of intensities with different phenomena. “Tin cry,” which occurs when tin is under tension or bending, is a typical example of AE on a small scale (Miller, 1936). An earthquake is another example of AE on a large scale (Katsuyama, 1994). The mechanism of AE generation is the same, whether it is a microcrack in a material or an earthquake. It is a release of elastic energy into AE waves by the formation of a crack in a solid. AE is used to nondestructively monitor structural integrity and characterize the behavior of materials when they undergo deformation, fracture, or both. Unlike ultrasonic or radiographic techniques, AE does not require external energy because the energy is released from the test object itself. The advantages of AE technique are presented, as follows;

1. The position of developing cracks can be determined. AE source can be determined from the time differences of AE signals among several AE transducers.

2. The classification and direction of cracks can be calculated by AE waveform analysis using moment tensor components.
3. The dynamics of the materials can be observed in real time.

The disadvantages of this method are presented, as follows;

1. It is often difficult to discriminate real AE signals from background noise during measurement.
2. For some materials, generation of AE does not occur until the material is loaded close to the proportional limit of the final failure.
3. The output signal of AE transducer is the combination of the AE source wave, propagation, and transducer response. For concrete, unlike metal materials, small AE events cannot be detected as AE signals because of considerable attenuation of AE waves during propagation, unless appropriate transducers are used.
4. For concrete, the wave velocities are 4 to 5 km/s for longitudinal, and 1.5 to 2 km/s for transverse. Since conventional AE source location technique assumes isotropic velocity, the source location, the most identifiable and beneficial factor of the AE technique for homogenous materials, is sometimes difficult to use in concrete.

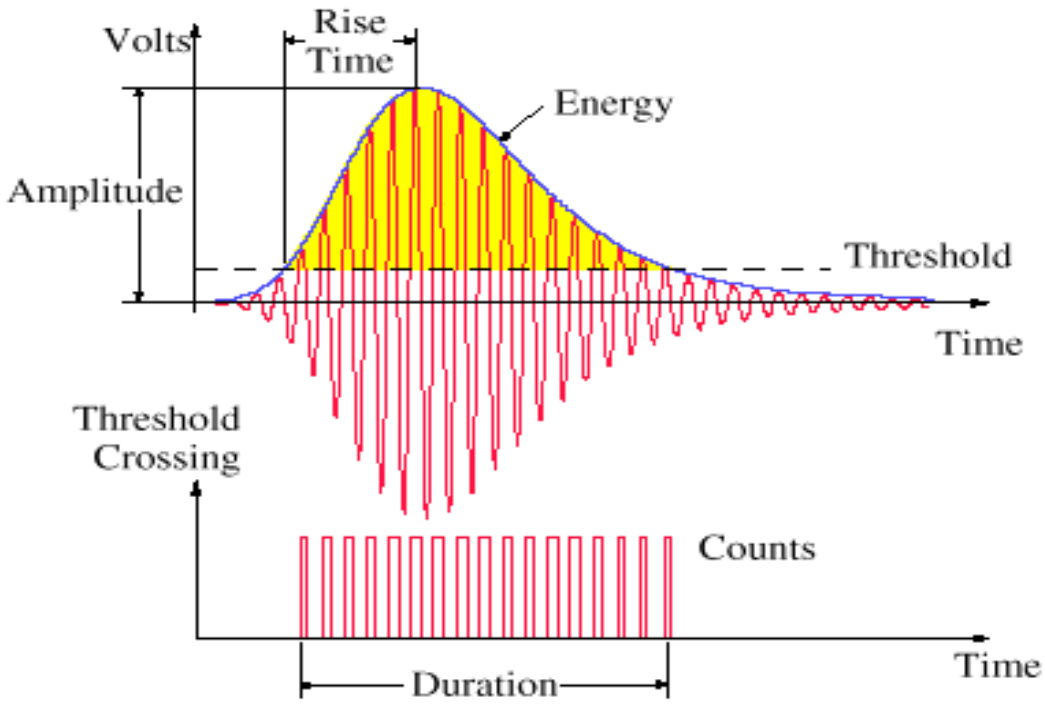

Figure 2.10 AE waveform parameters

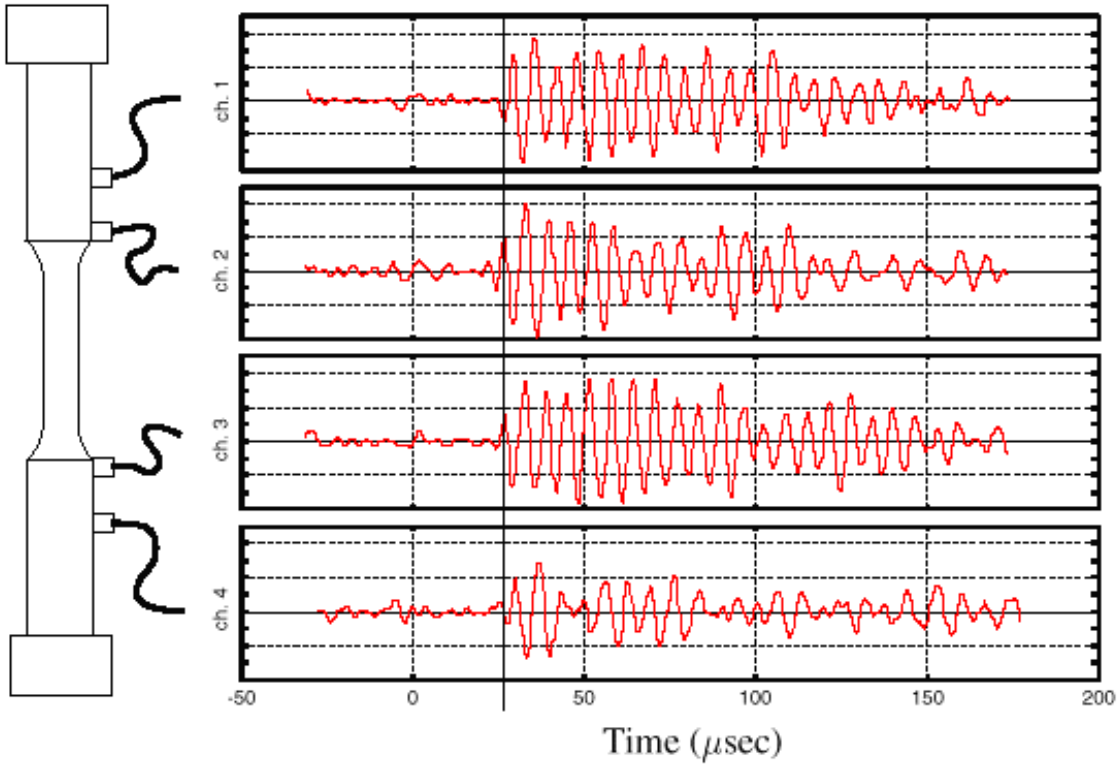

Figure 2.11 Investigation of the source location of AE signals by the arrival times of several AE sensors.

Measurement

(1) AE wave and signal wave

An AE wave is an elastic wave, having a wide frequency range (kHz to MHz), generated by the release of energy due to the formation of a micro-crack. AE signal is the output signal of AE equipment after the AE wave has been electrically processed. The frequency spectrum of AE wave is affected by the properties of the transducer, materials, and wave path. AE waveform is usually the overlap of longitudinal, transverse, Rayleigh, and reflected waves as shown in Figures 2.10 and 2.11. The AE waveform is highly affected by specimen dimension. When the specimen thickness is shorter than the wavelength, the maximum amplitude is governed by Lamb waves instead of body waves.

(2) AE transducer

The most important factor of AE measurement is the selection of the appropriate AE transducer, depending on the purpose of the measurement. It is also important to use the appropriate couplant to minimize energy loss transferred from the surface of the material. Couplant is defined as a material used at the substrate-to-sensor interface to improve the transmission of acoustic energy across the interface during AE monitoring (ASTM E1316). When surface mounting is difficult, wave guides can be used. These are solid wires or rods that link the surface being measured to a transducer. AE transducers are generally piezoelectric (PZT) devices that transform vibrations produced by elastic wave into an electrical signal (ASTM E1316). The dimension of the PZT element affects the frequency response of the transducer. The sensitivity of an AE transducer having a resonant frequency is generally higher than that of a non-resonant type. X-cut PZTs, used for most AE measurements, have the highest sensitivity in the Y-axis of the transducer. Periodic sensitivity checks of transducers are required (ASTM E1106 and E1781). To select the proper AE transducer, the sensitivity and frequency response should be taken into consideration. For a material with high attenuation, AE transducers of low resonant -frequency should be used. For AE wave analysis, flat

non-resonant transducers should be used. The velocity of most longitudinal AE waves is more than 4 km/s in concrete. Since wavelength is determined from the velocity divided by frequency, a higher frequency transducer gives better results for thin, small specimens. However, in materials having high wave attenuation, it is important to use the appropriate low resonant-frequency transducer.

(3) Signal processing

Signal processing requires several AE electronic components, including transducers, preamplifiers, filters, amplifiers, cables, and threshold and counting instrumentation (ASTM E750). Wave guides may be used in high temperature environments to get AE wave to the transducer, while, the preamplifier should be as close as possible to the transducer. The frequency spectrum of AE signal is the most practical way to determine the filter and amplifier selection. The level and quality of background noise determine the available amplifier/threshold and the lower frequency limit. The upper frequency limit is governed by wave attenuation. It is desirable to confirm the limitations of instrumentation for detecting AE in advance. Until recently, AE instruments were limited by data storage capability and processing speed. Recent developments in computer technology have greatly decreased these limitations.

(4) Data interpretation

The distance between AE source and the transducers affects results, particularly for materials like concrete. Before AE parameters are interpreted, the effects of transducers, system sensitivity, background noise, and material properties should be taken into consideration. Even though special precautions for isolating AE signals from background noise are taken, the distinction of AE from noise limits the interpretation. Monitoring the waveform, in addition to counting the signals, helps to distinguish AE from noise. In concrete, attenuation and wave velocity are different for longitudinal, radial, and tangential directions. Radial and tangential attenuation is larger than longitudinal attenuation. As for AE source location in concrete, the area where one transducer can

distinguish the signals from the background noise should be taken into the consideration.

Historical review of AE technique

The first documentation about the observation of AE phenomenon may have been made by Arabian alchemist Jabir Ibn Hayyan in the eight century, who was known also under the name of Geber. The book “Summa Perfectionis Magisterii” was published as English translation in 1678 (Nondestructive testing handbook, V.5, 1987). Kalischer (1882) noticed that rolled zinc ceased to give a ringing sound when struck after it was heated to 160-300^{o}C. Then, it could bent easily, and went bent it emitting a sounds like the cry of tin. Portevin and Chatelier (1923) reported that small sharp noise was clearly listened from a distance of several meters during discontinuous yielding and Luders-band formation in aluminum-copper-manganese alloys. Drouillard (1986, 1996) reviewed the development of AE technology from the time AE waves were first detected in rock, wood, and metal in the 1930s. AE research applied to mine timbers and research by Kishinoue using fracture of wood (Kishinoue, 1934, 1990). Kishinoue was the first person to record AE signals. In a Japanese article in 1934, Kishinoue described an experimental method to detect elastic shocks (AE) during bending of quarter sawn boards of Japanese cedar, pine, and cypress. He transferred the vibrations (AE) associated with the fracture of a board into an electric gramophone through a needle on the board. Signals were recorded on cinematographic film. The instrument was developed by Haeno (1930).

In contrast, Forster of Germany was the first person to detect and investigate AE. Forster detected a small sound during growth of plants using amplification and recording instrumentation (Reich and Forster, 1932). In the mid-1930s, he developed the system that had theoretically the same processing method as the currently used. Then he carried out the analysis of the formation of marten-site (Foster, 1936).

Large-scale AE events from fracture in mines have been identified as the rumbling sound that occurs before an actual cave-in. Katsuyama (1994) described the experience of a miner in Japan

in 1927, who escaped from a mine disaster after hearing rumbling prior to the cave-in. AE technique for monitoring the stability of rock masses in mines was initiated in the 1940s by Obert (1941, 1942) and Mason and others (1948). Obert performed investigations in mines to determine if rock bursts could be predicted. Using a microphone and amplification, he detected sub-audible noises of stressed rock as microseismic signals for predicting the rock movement preceding failure. The early AE work was in the preliminary stage until the work of Kaiser in the year of 1950 on metal at the Technische Hochschule Munchen in Germany. Kaiser conducted the tensile test of conventional engineering materials to determine what noises are generated from the specimens of these materials under loading. Thus AE was studied and the frequency level was found. Stress-strain behaviour and the frequencies of these materials under various stresses were examined. The important discovery of Kaiser was the irreversibility phenomenon named the Kaiser effect (Kaiser, 1953). Mogi (1962) studied AE generation in rock in relation to earthquakes.

After Kaiser's work, AE research progressed in the United States. Schofield (1958) first used the term acoustic emission, instead of previously used terms like stress wave emission, microseismic activity, and noise. He established the basic mechanism of AE under applied stress. In the 1960s, Green pioneered pressure vessel testing. This AE technique was used for rocket inspection in the United States (Green, 1985). Dunegan and others (1964) used AE equipment to detect defects in metallic vessels. Recent applications of AE to concrete engineering were reported around 1978 by M. Ohtsu. In the 1980s, Ohtsu (1982) applied the theory of elastodynamics to AE waveform analysis, to characterize crack kinematics of concrete. He proposed AE waveform analysis based on moment tensor analysis to identify crack type and crack orientation in concrete (Ohtsu and Ono 1984a, b; Ohtsu 1988a). Neural network and fuzzy theory are used to identify the signals of longitudinal waves (Inaba, 1994; Tiitta et. al., 2001).

The Acoustic Emission Working Group (AEWG) organized in 1967 has contributed to the development and distribution of AE technology throughout the world by organizing international symposia and participating in standardization activities. In addition to standards issued by the

American Society for Testing and Materials (ASTM), AE standards are issued by the American Society for Nondestructive Testing (ASNT), American Society of Mechanical Engineers (ASME), European Working Group on Acoustic Emission (EWGAE), Japanese Society for Nondestructive Inspection (NDIS), and, recently, the International Organization for Standardization (ISO) committee.

Publications are available in Japan on the fundamentals of AE in concrete (Katsuyama, 1994; Ogami and et. al., 1979; Ohtsu, 1988b). Ohtsu (1987a,b,c, 1988c, 1989, 1991) described AE analysis for application to concrete materials, and Katsuyama edited a book on in situ application of AE in metal, rock, concrete, and on-line monitoring of materials processing. Beattie (1983) described principles and instrumentation of AE. Kishi (1980a,b) reviewed studies on the strength evaluation of materials.

As an application of AE to fracture mechanics, the study of the fracture process zone (FPZ) in two-dimensional analysis by locating AE sources was conducted by Maji and Shah (1989). Li and Shah (1994) studied the localization of microcracks in unnotched concrete specimens. Maji and Shah (1989) applied AE location technique to detect the fracture process zone in concrete. It is also confirmed that AE waveforms can be synthesized by dislocation model (Ohtsu, 1982). At present, based on the eigenvalues analysis of the moment tensor, AE sources are classified into tensile cracks and shear cracks. The direction of crack motion is derived from the eigenvectors. The procedure is implemented as the SiGMA code. Crack orientation along with crack type can be determined by SiGMA procedure.

Moment tensor analysis of AE and development of SiGMA procedure

AE waves are elastic waves due to crack nucleation in concrete, which are formulated in a homogeneous medium. This is because the effect of heterogeneity is significant in only the case that the wavelengths are shorter than the sizes of heterogeneous inclusions. In concrete, wavelengths of AE waves are even longer than a few centimeters, which are obviously larger than the sizes of

aggregate. A crack can be modeled by crack-motion vector **b** and unit normal vector **n** to crack surface F as given in Figure 2.12. Crack motion is set to be b(y)***l***S(t), where b(y) represents the magnitude of crack displacement, **l** is the direction vector of crack motion, and S(t) is the source-time function of crack motion. From the generalized theory (Ohtsu and Ono, 1984a), AE wave motion **u**(x,t) can be represented,

$$u_i(x,t) = \int_F T_{ik}(x,x',t) * b_k(x',t)\, u_i(x,t) = \int_F C_{pqkl} * G_{ip,q}(x,y,t) * [b(y) l_k S(t) n_l \, dS$$

$$= G_{ip,q}(x,y,t) * m_{pq} * S(t). \qquad 2.44$$

Where $G_{ip,q}(x,y,t)$ are the spatial derivatives of Green's functions and * denotes the convolution integral. C_{pqkl} are elastic constants. The following integration over crack surface F leads to the moment tensor m_{pq},

$$\int_F C_{pqkl} * [b(y) l_k] n_l \, dS = [C_{pqkl} \;\; l_k n_l] \; [\int_F b(y) \, dS] \;\; = [C_{pqkl} \;\; l_k n_l] \; \Delta V = m_{pq} \qquad 2.45$$

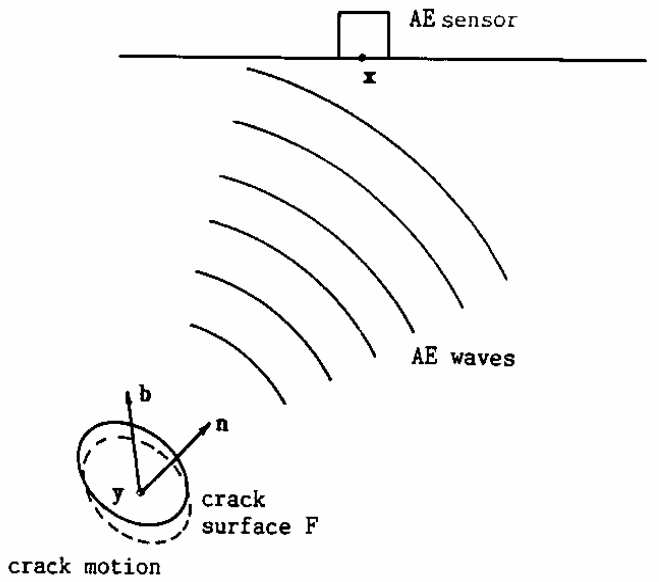

Figure 2.12 Generation of AE waves due to cracking

In the case of an isotropic and elastic material, the moment tensor components are represented as,

$$m_{pq} = (\lambda l_k n_k \delta_{pq} + \mu l_p n_q + \mu l_q n_p)\Delta V = C_{pqkj}\, bl_k\, n_j$$

$$m_{pq} = \begin{bmatrix} \lambda b_k n_k + 2\mu b_1 n_1 & \mu(b_1 n_2 + b_2 n_1) & \mu(b_1 n_3 + b_3 n_1) \\ \mu(b_2 n_1 + b_1 n_2) & \lambda b_k n_k + 2\mu b_2 n_2 & \mu(b_2 n_3 + b_3 n_2) \\ \mu(b_3 n_1 + b_1 n_3) & \mu(b_3 n_2 + b_2 n_3) & \lambda b_k n_k + 2\mu b_3 n_3 \end{bmatrix} \Delta V \qquad 2.46$$

These components in Eq.2.46 are illustrated in Figure 2.13.

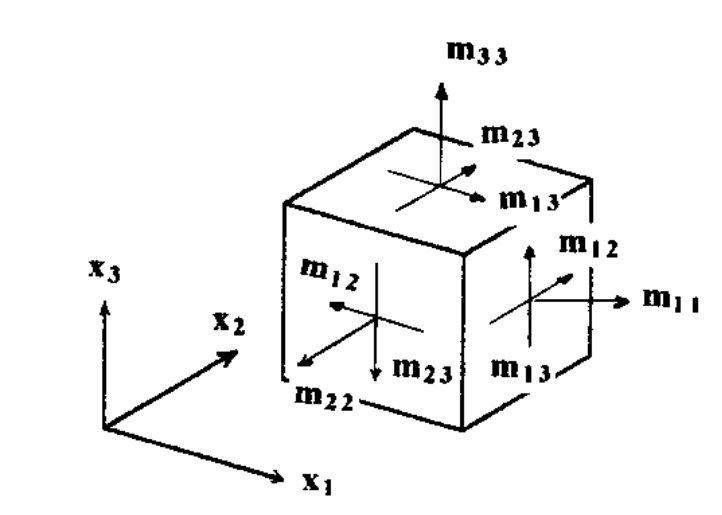

Figure 2.13 Moment tensor components.

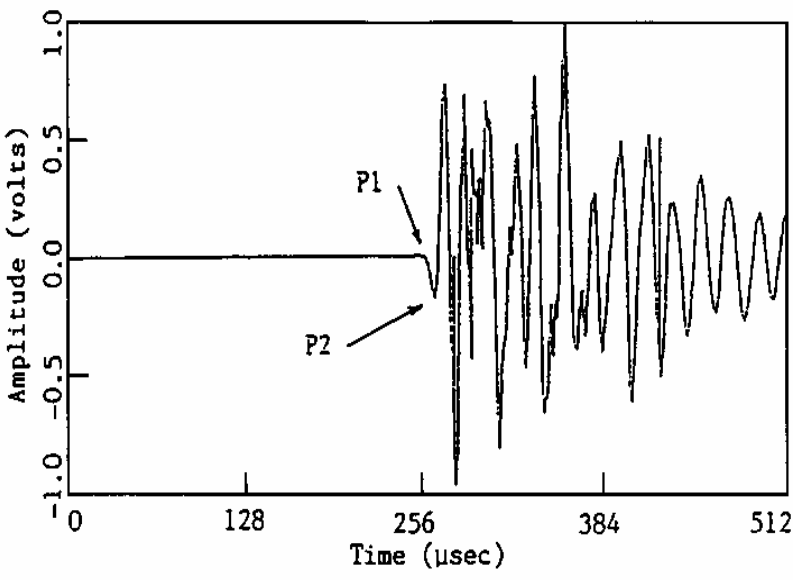

Figure 2.14 Recorded AE waveform.

Here λ and μ are Lame constants. $l_k n_k$ follows the summation convention. Normal component m_{11}, m_{22}, and m_{33} result in the dipole forces, while m_{12}, m_{23}, and m_{13} represent double-couple forces. In SiGMA (Simplified Green's functions for Moment tensor Analysis) procedure, Eq.2.44 is simplified, taking only into account the first motion A(x) of AE waveform as,

$$A(x) = Cs / R \; \mathrm{Ref}\, (\boldsymbol{t},\boldsymbol{r})\; r_p\, m_{pq}\, r_q, \qquad 2.47$$

Since the moment tensor is symmetric and of the 2nd order, the number of independent unknown m_{pq} is six. To solve Eq.2.47, two parameters of the arrival time (P1) and the amplitude of the first motion (P2) are read visually from recorded AE waveforms, by displaying them on the CRT as seen in Figure 2.14.

The location of the source is determined from the arrival time differences. Then, Eq.2.47 is solved to determine moment tensor component m_{pq}. It is noted that, prior to the solutions, calibration coefficient Cs in Eq.2.47 should be relatively determined to compensate the sensitivity of AE sensors. In order to estimate errors of the moment tensors obtained by SiGMA procedure, an error analysis was previously conducted, assuming location errors (Ohtsu, 1991). It was then found that the accuracy of solutions was highly dependent on the geometrical configuration between the sensor array and AE sources. Furthermore, it was realized that the most errors could be introduced from misreading the first motions. To select reliable solutions, therefore, a post-analysis was developed. Theoretical AE waveforms at actual AE sensor locations can be synthesized by Eq.2.44. In the computation, the data of AE source location and moment tensor components determined by SiGMA procedure are substituted. For simplicity, full-space Green's functions $G_{ij}(x,y,z)$ are employed, taking into account the reflection coefficients and the calibration coefficient. Although one procedure was proposed (Go et al., 1984), the comparison of AE waveforms with theoretical waveforms at all channels is time-consuming and is not quantitative. Applying SiGMA procedure to theoretical first motions, AE sources, of which crack kinematics in the post-analysis are in good

agreement with those of the original SiGMA analysis, are selected as reliable solutions.

Crack analysis by AE-SiGMA procedure

(1) Classification of crack type

The classification of cracks can be performed from the eigenvalues of the moment tensor. Solving the characteristics equations of Eq.2.46, three eigenvalues are obtained, as follows,

$$\text{The maximum eigenvalue: } e_1 = \mu\left(\frac{l_k n_k}{1-2\nu}+1\right)\Delta V$$

$$\text{The intermediate eigenvalue: } e_2 = 2\mu\nu\left(\frac{l_k n_k}{1-2\nu}\right)\Delta V \qquad 2.48$$

$$\text{The minimum eigenvalue: } e_3 = \mu\left(\frac{l_k n_k}{1-2\nu}-1\right)\Delta V$$

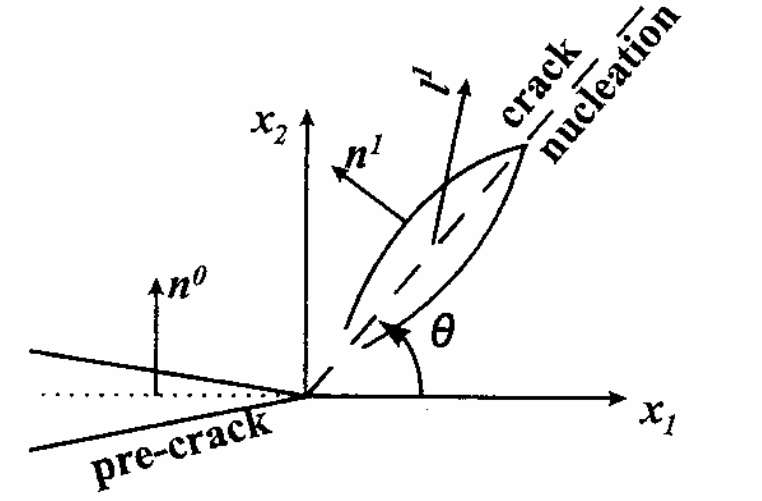

Figure 2.15 Configuration of crack extension.

The relation $\lambda=2\mu\nu/(1-2\nu)$ is applied, where ν is Poisson's ratio. Corresponding to nucleation of each crack in Figure 2.15, these eigenvalues are derived. Setting shear contribution of the moment tensor as X, three eigenvalues of the pure shear crack become X, 0, -X, because $l_k n_k = 0$. In the case of the pure tensile crack, three eigenvalues are decomposed into the deviatoric components (Y, -Y/2, -Y/2) and the isotropic components (Z, Z, Z), setting the maximum deviatoric tensile component as

Y and the isotropic tensile component as Z. In the case of a general crack, it is assumed that the eigenvalues of the moment tensor are composed of the shear crack and the tensile crack as shown in Figure 2.16. Because only relative values are required for the classification of crack, Eq.2.48 is normalized and becomes,

$$\begin{aligned} 1.0 &= X + Y + Z \\ \frac{e_2}{e_1} &= 0 - \frac{Y}{2} + Z \\ \frac{e_3}{e_1} &= -X - \frac{Y}{2} + Z \end{aligned} \qquad 2.49$$

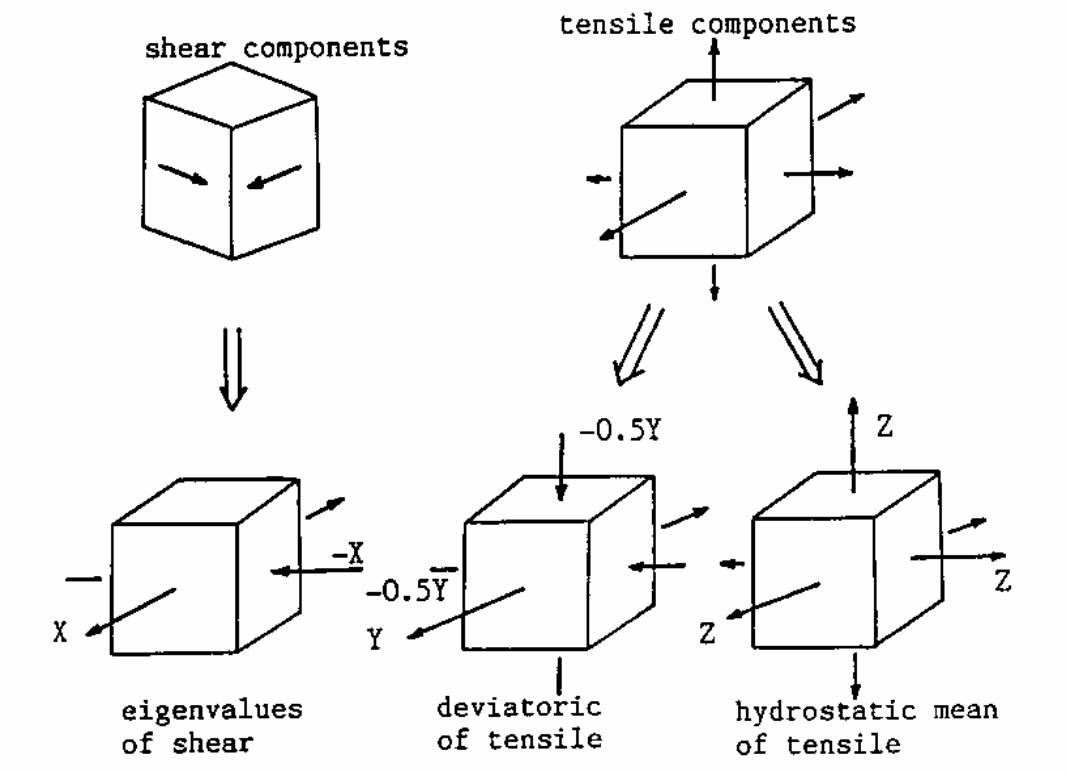

Figure 2.16 Unified decomposition of the eigenvalues of the moment tensor.

It was pointed out that the ratio X could become greater than 1.0 in the case that both Y and Z are negative (Suaris and van Mier, 1995). It happens only if the scalar product $l_k n_k$ is negative. Recollecting the scalar product, the three ratios become well-posed. From solutions of Eq.2.49, AE sources for which the shear ratios X are smaller than 40% are classified as tensile cracks. AE

sources of the shear ratio X greater than 60% are referred to as shear cracks. In between 40% and 60%, AE sources are classified as mixed mode.

(2) Orientation of crack motion

In the eigenvalue analysis, three eigenvectors are also determined. These can be represented by using vectors **l** and **n** as,

The eigen vector for $\boldsymbol{e_1}$: **l** + **n**,

The eigen vector for $\boldsymbol{e_2}$: **l** x **n**, 2.50

The eigen vector for $\boldsymbol{e_3}$: **l** - **n**.

Where x means the vector product. In SiGMA procedure, unit vectors: $\boldsymbol{e_1}$, $\boldsymbol{e_2}$, and $\boldsymbol{e_3}$ of directions (**l** + **n**), (**l** x **n**), and (**l** - **n**) are determined, respectively. The vectors **l** and **n** are, then, recovered from the following relations,

$$\mathbf{l} = [(2+2l_k n_k)^{1/2}\, \boldsymbol{e_1} + (2-2l_k n_k)^{1/2}\, \boldsymbol{e_3}]/2$$

$$\mathbf{n}=[(2+2l_k n_k)^{1/2}\boldsymbol{e_1}-(2-2l_k n_k)^{1/2}\boldsymbol{e_3}]/2 \qquad 2.51$$

Summary

In this chapter, the state of the arts on fracture mechanics of concrete and AE-SiGMA are presented. Obviously, many aspects of the field are still unclear, and many questions related to the fracture process remain unanswered. A lot of research is required to clarify theses problems and to explain the underlying causes for the contradictory conclusions of the different researchers regarding the same problem. The presented discussion on the concept of crack propagation in concrete in mode I fracture and mixed-mode fracture reveals the applicability of LEFM to concrete. For the measurement of the valid fracture toughness, it is necessary to take into account the fracture process zone nucleated ahead of the crack tip. It is known that the following questions concerning mixed-mode fracture remain unanswered.

1. Is the crack growth governed only by a mode I deformation mechanisms? In other words, is mode II deformation important?
2. Does mixed-mode fracture energy exist?
3. What influence does the loading sequence have on crack propagation?

A part of answers to these questions are tried to be resolved in the present study. Thus, some new lights and explanations is to be given, associated with the results achieved in the following chapters.

AE sources can be analyzed by SiGMA procedure, and are classified into tensile cracks and shear cracks or mixed-mode. Crack locations, crack types and crack orientations are determined. The classification of the crack type based on the shear ratio in the SiGMA procedure could contribute to discriminate the dominant mode of the fracture. The results presented here could become valuable in response to the improvement of the understanding of cracking mode in concrete.